Thesis for the degree of Master of Science in Physics

Prototype tests and pilot experiments for the R^3B scintillator-based detection systems

RONJA THIES

Supervisor: Thomas Nilsson

Department of Fundamental Physics
CHALMERS UNIVERSITY OF TECHNOLOGY
Göteborg, Sweden 2011

Prototype tests and pilot experiments for the R^{3}B scintillator-based detection systems

RONJA THIES

Thesis for the degree of Master of Science in Physics

Department of Fundamental Physics
CHALMERS UNIVERSITY OF TECHNOLOGY
SE-41296 Göteborg
Sweden
Telephone: +4631-7721000
www.chalmers.se

Cover:
Sketch of the Crystal Ball detector and a γ-source, displayed together with a spectum obtained from a ^{60}Co source during the calibration of the Crystal Ball.

Chalmers Reproservice
Göteborg, Sweden 2011

Prototype tests and pilot experiments for the R^3B scintillator-based detection setup

RONJA THIES
Department of Fundamental Physics
Chalmers University of Technology

Abstract

Understanding atomic nuclei is still an unaccomplished task and radioactive ion beam experiments aim at achieving this. Complex detector systems are the essential tool of such experiments and determine what kind of data can be collected and their quality.
The LAND-setup at the heavy ion research facility GSI is designed for experiments with exotic nuclei. Developing GSI into the larger facility FAIR, the LAND-setup of GSI will become the R^3B (Reactions with Relativistic Radioactive Beams) setup. This means explicitly that new detectors and a new magnet are being designed and built. Experiments with the present setup thus serve not only for physics research but also for prototype testing, giving clues how detectors need to be improved.
This thesis takes a close look at the calibration of the γ and proton detector, Crystal Ball, of the LAND-setup. Three efficiency calibration methods are automated and tested. It is clearly identified which method should be used for the analysis of the present experiments. Furthermore, methods which will be applicable to the new, highly granular γ and proton detector for R^3B, are identified for different scenarios.
As a second part of this work an option for the read-out system of the planned neutron detector consisting of plastic scintillator paddles has been tested. This is read-out by Multi-Pixel-Photon-Counters, MPPCs, which are solid state photomultipliers. These are expected to have very good timing and photon-counting ability while being much cheaper than PM-tubes. The two proposed realizations of the preamplifier circuit for the MPPC did not work as expected; probably because the preamplifier specified is too slow.

Keywords:
Crystal Ball, Calibration, Efficiency, γ-detector, Proton detector, MPPC

Contents

1 Introduction

Nuclear physics strives to understand the atomic nuclei. Nuclei are quantum-mechanical many body systems, the nucleons basically interacting via strong, electromagnetic and weak force[1)]. While the electromagnetic and the strong force govern the nuclear structure, the weak and strong force govern the decay of a nucleus. With both the strong force and the formation of nuclei not yet being fully understood, this research field has still a lot of open questions to be answered.

This is what nuclear physics aims at, understanding how nuclei are formed, and what their properties are, which is closely related to understanding the strong interaction. This will also lead to a better understanding of the formation of heavy nuclei in astrophysical processes.

Stable and unstable abundant nuclei turn out not to tell the whole picture about nuclei, and thus it is necessary to study also nuclei towards and beyond the driplines[2)]. This task comes with a few problems as the nuclei may have lifetimes as short as a tiny fraction of a second[3)], and thus creation of and experiment with the nuclei need to be close together (in time). This issue is best solved by working with radioactive ion beams (RIB). Such beams are created from beams of stable nuclei, and have energies up to a few GeV/u which gives a range of possibilities to investigate the created unstable

[1] They do of course also interact via gravity, which is negligible though in comparison to the other interactions on the nuclear scale.

[2] Dripline is a name for the lines on the nuclear chart beyond which the nuclei are not bound. There exist two of them, the proton dripline on the proton rich side which marks the points at which addition of protons will lead to unbound nuclei and the neutron dripline, which marks where addition of neutrons will lead to unbound nuclei.

[3] I still search for the nuclear physics definition of a nucleus. Chemists define a nucleus to a chemical element via IUPAC, in Ref. [1], to have a lifetime of at least 10^{-14} s, the time it takes (roughly) for a fully ionized atom to acquire its electrons.

nuclei. One of them is to collide them with a target and record their break-up which gives information about the structure and properties of the nuclei. In order to be able to infer the information on structure, complete kinematics experiments are a powerful tool. Complete kinematics means that the incoming nucleus and its velocity (vector) are recorded and that all outgoing particles (fragments, protons, neutrons, γ's) and their respective momenta (vectors) are detected. The detection of all incoming and outgoing particles is quite complicated, employing more than ten detectors, all together having several thousand channels, in the setup this thesis is concerned with. This leaves calibration of the detectors a nontrivial exercise which should employ automatic routines as far as possible.
Detectors thus play a key role in this research field, where improving detectors directly pays off in physics results and is therefore also a general objective and focus when designing new detectors. The existing facilities will thus not only enable physics research but also act as prototypes for next-generation experiments, telling where and what kind of improvements are necessary in order to allow digging deeper into physics.
This is especially timely as one of the leading facilities in this field, GSI, is to transform into an even larger facility, FAIR (Facility for Antiproton and Ion Research), and in the course of this process, many new detectors are being built.

1.0.1 Outline of the thesis

In this work a γ and proton detector (the Crystal Ball detector of the LAND setup) is being calibrated, with an outlook on calibration of its successor. Furthermore, an alternative scintillator read-out for the planned new neutron detector (NeuLAND) of that same setup is tested.
In the following an introduction to the physical theoretical background and the basic principles of scintillating detectors is given. The experimental setup this thesis deals with (LAND-setup) and its hosting facility GSI are described in Sec. 1.3. This is followed by the chapter (Ch. 2) about the γ and proton detector calibration and the chapter (Ch. 3) about the neutron detector read-out. In the last chapter results are discussed and a summary is given.

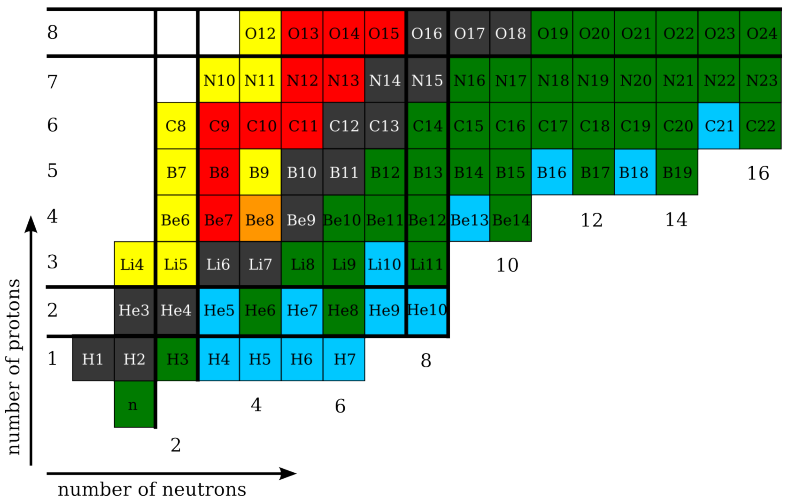

Figure 1.1: Excerpt from the nuclear chart, all information taken from Ref. [2]. Dark grey indicates stable nuclei, all other nuclei are unstable. The other different colors indicate the main decay processes: green - β^- decay, blue - neutron emission, red - electron capture and β^+ decay, yellow - proton decay, orange - α decay.

1.1 Theoretical Background

Let us start by taking a look at the nuclear chart, the map a nuclear physicist uses to order the jungle of isotopes[4)], an excerpt from it displayed in Fig. 1.1. The dark grey nuclei are stable, all others are not.

So why are certain nuclei stable while other are unstable? The traditional best attempt to explain this is the nuclear shell model [3–5], working similarly to the atomic shell model. This also introduces the magic numbers, indicated by the thick black lines in Fig. 1.1, which describe the number of protons (neutrons) for which a shell (of the nuclear shell model) is filled. This is characterized by the separation energy[5)] dropping sharply after filling a "shell", while it otherwise increases. This has been measured and the magic numbers determined. Due to the fact that protons and neutrons are different particles[6)], though interacting, they each fill up their own level diagrams. This explains

[4] It is similar to the Periodic Table used by chemists, but instead of focusing on the chemical properties derived from the electrons of an atom it focuses on the nuclear properties.

[5] This is the energy it takes to remove one or two nucleons (of same isospin), depends how measured. Usually the two-nucleon separation energy is given due to pairing.

[6] which manifests itself in different isospin quantum number

why stable nuclei consist of about same amounts of protons and neutrons, as this is energetically favored[7], and also why nuclei further away from the line of stability are more short-lived than the ones close to it, with the reservation for exceptions, due to pairing or clustering effects for example. There are however unsolved questions in and even contradictions to the shell model, especially concerning nuclei with extreme isospin (i.e. asymmetric nuclei, where one sort of nucleons dominates).
The deviations from the description by the shell model are two (probably related) manifestations; the magic number, i.e. the amount of protons/neutrons enhancing stability of a nucleus seems to be moving when close to the driplines [6]. The other effect is the structure of nuclei changing close to the dripline compared to stable nuclei. This manifests strongly in e.g. halo nuclei. These are nuclei where one or two nucleons are located outside the core (consisting of the other nucleons) forming an essential two- (three-)body structure of the core. This is classically forbidden [6] and only possible for very weakly bound nucleons as otherwise the wavefunction of the nucleon could not extend out of the core. This is one reason why these nuclei are studied extensively.
Another reason to study light exotic nuclei is that they can provide information of element formation in astrophysical processes. The abundances of elements in the universe are not fully explained yet by the known processes. Studying e.g. neutron capture cross sections of light neutron-rich nuclei might improve the understanding [7].

1.2 Scintillation detectors

Scintillating detectors emit light proportional[8] to the energy deposited in it by primary or secondary charged particles. The emitted light is collected by photomultipliers and transformed into electric pulses, a sketch illustrating the setup is shown in Fig. 1.2.
The main specification, as already mentioned, for a material to work as a scintillator detector is that it needs to be luminescent, i.e. it re-emits energy it has absorbed (from particles, light, etc.) as (visible) light in frequencies it is transparent to. The

[7] This applies for light nuclei with "few" protons/neutrons, for larger amounts the potential of the proton is different, due to the electromagnetic force, stable nuclei have slightly more neutrons than protons for heavy elements.
[8] At least they are supposed to. Quenching effects at high energy deposits destroy this proportionality.

transparency is important as otherwise the light cannot travel through the scintillating part of the detector to the parts where it is collected. Another factor is the time between excitation (due to absorption of energy) and reemission of the energy, called τ, which should be as short as possible in order to get the fastest response possible, as illustrated in eq. 1.1. For most materials one can neglect the time required to excite it and thus the emission of light can be described according to Ref. [8] as:

$$N = \frac{N_0}{\tau} \cdot e^{\frac{-t}{\tau}} \tag{1.1}$$

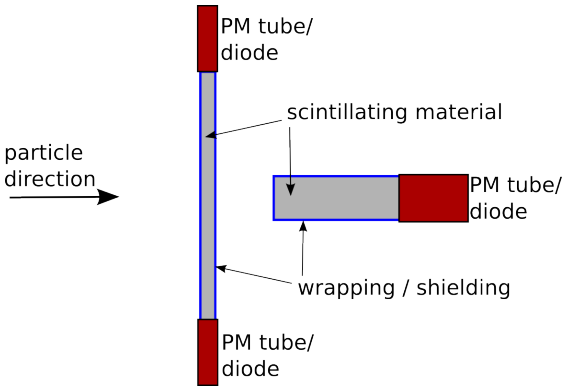

Figure 1.2: Illustration of the two basic ways scintillators are used as particle-/γ- detectors. The left arrangement is used for timing, position and ΔE measurements, the right one for full energy measurements also providing time and (often coarse) position.

where N is the amount of emitted photons at time t and N_0 the total amount of photons emitted. Some materials also have more than one process of de-excitation via emission of light, leading to two and even three different time constants and thus two (three) superposed exponential decays.
It is of course also important that the light-emitting de-excitation is sufficiently probable such that one gets enough light output and that the light has a wavelength which is detectable with photomultipliers [8].
There are different material types which can be used as scintillators characterized by different (de-)excitation processes. The first big group are organic scintillators, often divided into crystalline, liquid and plastic, the latter of this group used most often in nuclear physics [8]. In these materials, the delocalized π-electrons are excited to higher energy levels when the material absorbs energy. These levels have a number of vibrational modes (of the molecule) and the de-excitation from the first excited state usually goes to higher-lying vibrational modes of the ground state causing the light emitted to have a slightly larger wavelength than required for exciting the electrons from the ground state to an excited state. This is due to the fact that de-excitation of the vibrational modes to the vibrational ground mode is radiationless, but most molecules are in the vibrational ground mode. Thus there are very few molecules which could absorb the

emitted light.
The other major group are inorganic crystals, often insulators. For them the energy deposited excites charge carriers either to the conduction band or to an exciton state. These de-excite via levels introduced by impurities for which de-exitation is allowed. Some of these transitions might be radiationless and thus the energy can be lost. Further, seldomly used materials are glasses and gases (mainly noble gases).
The schematic drawing in Fig. 1.2 illustrates the standard setups of scintillator detectors, at one or two ends of the scintillator material, light collectors are mounted. Usually PM-tubes are employed as light collectors, but photo-diodes in various forms are also used and becoming more popular. One example of the diodes, the so called multi-pixel photon counter (MPPC) is described in more detail in chapter 3. The design of scintillating detectors varies largely depending on their purpose and already in the LAND-setup (see Sec. 1.3) scintillating detectors with significantly different properties are employed. Bulk-like scintillators are used for calorimetric purposes of neutrons (LAND) and protons (Crystal Ball). Much smaller volumes of scintillator material are used for tracking detectors (like the SSDs or POS). But scintillating detectors are also used for other purposes like γ-ray spectroscopy where they might actually only take volumes of a few cubic centimeters.

1.3 The experimental setup: LAND

The so-called LAND-setup is located in Cave C at GSI (GSI Helmholtzzentrum für Schwerionenforschung GmbH) at Darmstadt, Germany. Its name is derived from the neutron detector of this setup, called LAND (Large Area Neutron Detector). This setup will transform into the R^3B setup (Reactions with Relativistic Radioactive Beams) during the coming years, while GSI will develop into an international facility called FAIR.
At GSI research with heavy ions is performed on several different topics with stable and radioactive beams. At the LAND-setup break-up reactions of radioactive nuclei are observed in complete kinematics, i.e. detecting the momenta and type of all outgoing (and incoming) particles. Depending on the requirements of each experiment, the setup is modified accordingly. Therefore, in this work referring to the LAND-setup refers to the LAND-setup of the S393 experiment. In the following a brief description of the GSI

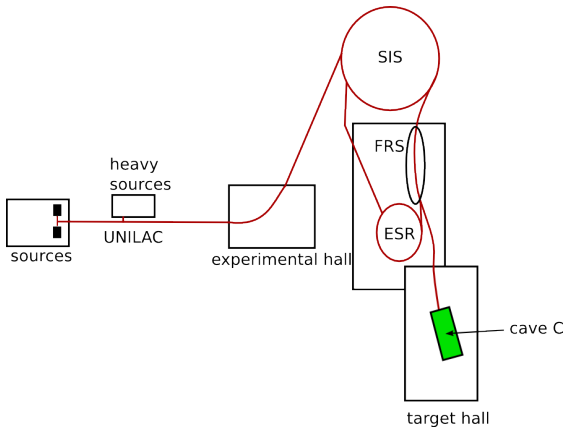

Figure 1.3: Sketch of the experimental and accelerator facilities at GSI. Beamlines are marked in red. The FRS (black ellipse) and Cave C (green rectangle) are indicated. Not to scale.

facility is given, followed by a short discussion of the production of the radioactive beams used at S393. The last part of this section presents the LAND-setup, i.e. the detectors and their arrangement.

At GSI, high intensity ion beams are produced and directed to experiments located in three experimental areas. These are situated at different accelerator stages, as can be seen in Fig. 1.3. The "experimental hall" is located after the first accelerator, the UNILAC, thus experiments at Coulomb barrier energies with high-intensity non-radioactive beams are conducted there. If the ions are not aimed for the experimental hall, they are guided to the SIS (SchwerIonen Synchrotron, heavy ion synchrotron) accelerating the ions to relativistic energies. After extraction from the SIS, the ions can travel two ways. Either they can be guided directly, or via the FRS (FRagment Separator) to the ESR (Experimental Storage Ring) and the target hall. The FRS produces the radioactive ion beams from the incoming stable beam by letting the stable beam impinge on a production target, where due to the collisions of the ions with the target nuclei, they fragment[9)]. This gives ions of all sorts lighter than the incoming ions. In order to sort out the wanted ion(s) which is supposed to arrive at the experiment, sending the fragments through a dipole magnet sorts out the right momentum-to-charge ratio, after

[9]Fission and spallation reactions do also take place, but in this work one uses the fragmentation reaction products.

the magnet the fragments pass through a degrader slowing them down proportionally to their charge number[10]. Subsequently, the magnet behind is adjusted to the velocity change of the wanted charge, thus passing fragments with the right charge. This method is not exclusive such that usually several species of ions are sent to an experiment, ions with up to a ΔZ=9 and up to 4 isotopes of one species were recorded in S393, allowing experiments with several ion species simultaneously.
Behind the FRS the three other experimental sites are located, each having its bending magnet being the last in the FRS respectively, i.e. the last bending magnet is different for the different experimental sites. The closest experimental site is S4 where the PRESPEC experiment is located. The next (following the beamline) is the ESR (Experimental Storage Ring) which can be used to store and observe the created ions. The third, the "target hall", hosts several experimental sites where the beam is shot onto a reaction target and observed by different detector arrangements. There also the LAND-setup is located in Cave C, marked green in Fig. 1.3.
Recapitulating, for the LAND experiment stable ions are extracted from one of the sources (in S393 it was ^{40}Ar) and accelerated in the linear accelerator UNILAC, subsequently guided into the SIS where they are accelerated to relativistic energies (to 490 MeV/nucleon for S393) extracted and sent through the FRS. At the FRS the stable beam is shot onto the production target (for S393 it was made of beryllium and had 4011 mg/cm^2) in order to create unstable isotopes. Separating the wanted charge-to-mass ratio of all reaction products is also done at the FRS, guiding the created beam of radioactive ions to the experiment in Cave C.
When coming from the FRS the beam traverses two incoming beam plastic scintillator detectors at the positions S2 and S8 of the FRS which are situated in the middle and exit foci of the FRS respectively. They will be referred to as S2 and S8 further on. Together with an incoming beam tracking detector (POS, see below) situated in the cave, these give information about the velocity of the incoming ions via the time of flight (ToF). All other detectors used for the experiments are situated inside Cave C.

The LAND-setup in Cave C is supposed to enable measurement of complete kinematics of all particles. To achieve that, the detectors are arranged as presented in Fig. 1.4. In front of the target, two beam-tracking detectors are located: first the POS, a plastic

[10] For light ions, as in the present experiment, no degrader is used. The scintillating detector suffices as degrading material.

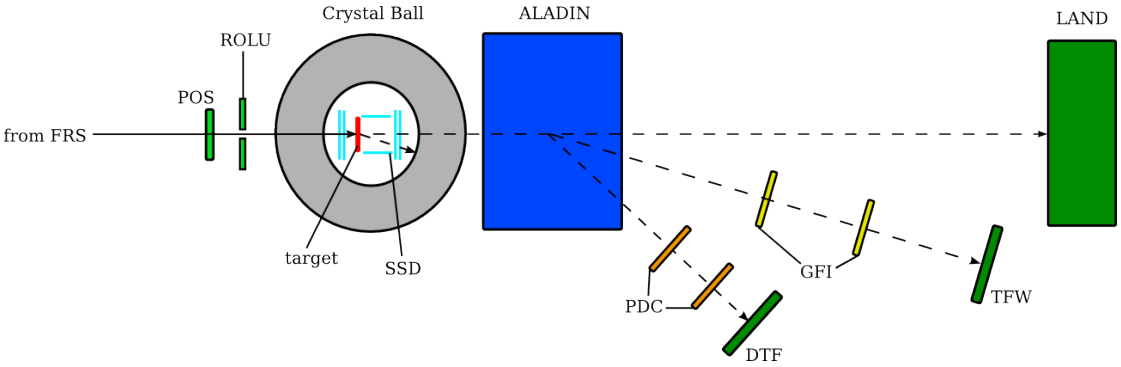

Figure 1.4: Schematic drawing of the detector setup at Cave C. See text for a detailed description. Not to scale.

scintillator across the beam pipe with a PM-tube at each of the four sides, thus capable of position sensitivity additionally to timing. It is most important for timing though, giving the global start and together with S2 and S8 the velocity of the incoming ions. It is followed by the ROLU ("Rechts-Oben-Links-Unten", right-up-left-down) which helps to determine and define the beam size. It consists of four scintillator plates, movable in and out of the beamline. As it works as a vetoing detector, all ions that deposit energy into it are vetoed by its trigger. Thus by moving the plates in and out one can define how large the spread of the beam is allowed to be. Except for two sheets of the SSD detector described later, these are all the detectors used for incoming beam determination. All the following are used to detect the particles created by scattering the beam at the target.

Around the target sits the first outgoing particle tracking detector (and partly incoming beam tracker), the SSD (Silicon Strip Detector), made of very thin silicon strips, providing position sensitivity and ΔE measurement. Two layers made of these strips are in front and back of the target each, and four as a box directly behind it, covering the directions perpendicular to the beam, as illustrated in Fig. 1.4. Around the target and the SSD, the Crystal Ball is situated, being a large array of scintillating crystals made of NaI built to detect γ's in 4π and protons in forward direction, though the full forward angle up to about 7.5° from the beam direction contains no detecting crystal, as the beampipe goes through there. It provides a measure of the total energy of the particles detected (as it is supposed to stop them) and has an angular resolution of about 15°. The Crystal Ball is described in further detail in chapter 2.

Particles which were not scattered strongly pass through the opening of the Crystal Ball and traverse the magnet ALADIN (A LArge DIpole magNet) in which they are bent according to their charge-to-momentum ratio. Thus, neutrons fly straight through it and hit LAND (Large Area Neutron Detector) which is standing farthest away from the target but is the only detector standing in the beam axis behind ALADIN. It is made of plastic scintillators and iron which is used as converter in order to increase the interaction rate of the neutrons.
The other detectors behind ALADIN are situated at an angle to the beam line corresponding to the kind of particles they are supposed to detect. Thus at small angles from the beam axis are the detectors for fragments, two scintillating fiber detectors with position sensitive PM-tubes as read-out, GFIs (Grosser FIber detektor, large fiber detector), horizontal positions of the outgoing ions, situated behind each other. They are followed by the TFW (ToF Wand, ToF wall) giving a ΔE measurement and their timing, additionally it also provides the position. It is made of plastic scintillator bars with PM-tubes at each end.
At larger angles, where one expects the protons which were not detected in the XB[11)] there are two drift chambers behind each other, giving a detailed position measurement. Following is the DTF (Dicke ToF wand, thick ToF wall) similar to the TFW, yielding ΔE, timing and position measurements. With these detectors one can thus determine kinetic energy, charge and mass of the in- and outgoing particles, thus called a complete kinematics measurement. More detailed information on each detector can be found on the *land02*-homepage [9].

[11] Those which are scattered forward at an angle smaller than 7.5° from the beam direction such that they do not penetrate the Crystal Ball.

2 The Crystal Ball

The Crystal Ball detector is a veteran 4π-γ-detector which has been upgraded to detect also protons at almost the full forward half-sphere. The detector is a spherical shell with an inner radius of 25 cm, comprised of 162 NaI crystals of four different shapes of which one is pentagonal (12 crystals, shape A) and the other three are hexagonal (150 crystals, shapes B, C and D). Each crystal is 20 cm long and covers the same solid angle.[10, 11] A schematical drawing shown in Fig. 2.1 illustrates this. At the outer side of each crystal sits a PM-tube converting the scintillation light into electronic pulses. The proton read-out was realized for 64 crystals by also reading out the signal of their PM-tube at its last dynode. Thereby the amplification was diminished such that, if a proton is detected, instead of an overflow (as in the γ branch, i.e. at the pickup anode) an unsaturated signal with energy-dependent peak height is read out. More detailed information on the proton read-out can be found in Ref. [12]. Signals from the PM-tubes are processed according to the diagram shown in Fig. 2.2. Clusters of 16 crystal are connected to one MSCF-16 module, each to one channel. In there the pulses are duplicated and processed by a timing branch and an energy branch. In order to digitize the pulse amplitude, it is treated by a shaper and passes through the baseline restorer, which was switched off during most of the S393 (and the whole

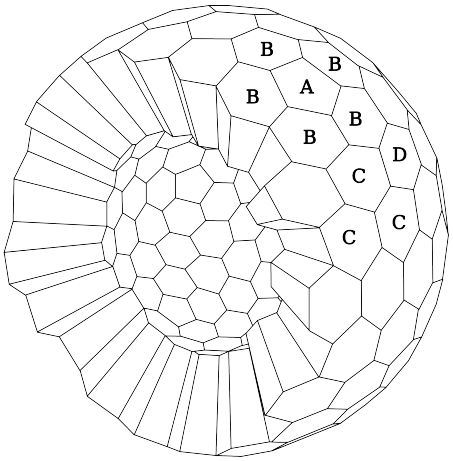

Figure 2.1: Schematic drawing illustrating the XB crystal structure. The letters label the different crystal shapes.

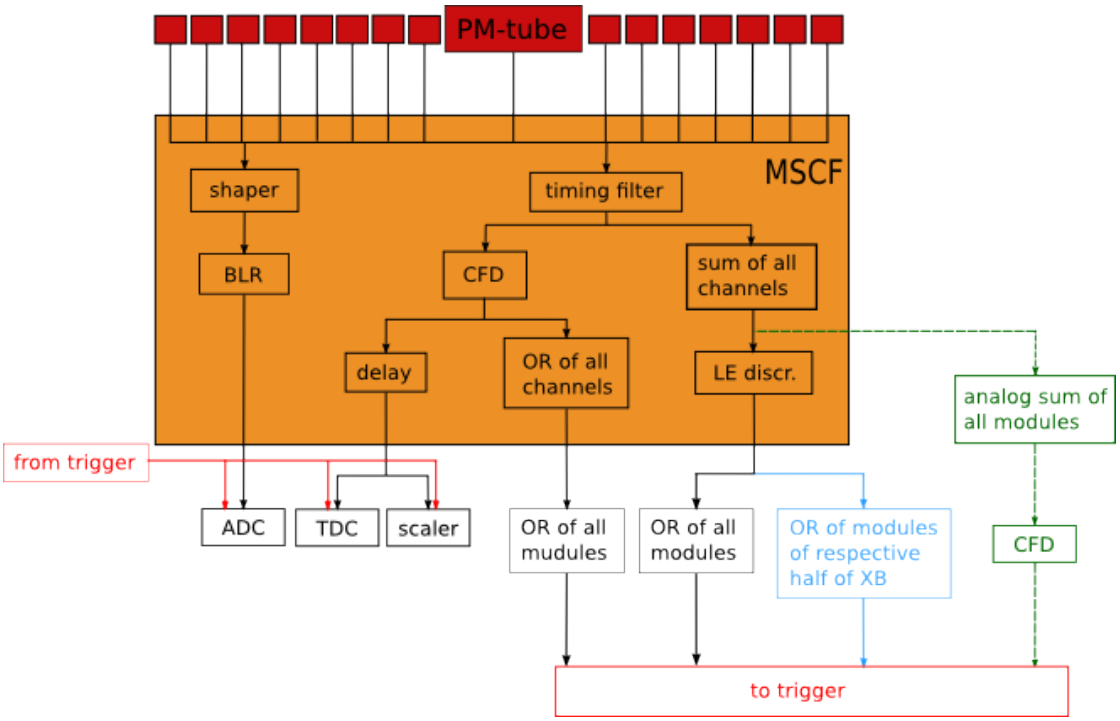

Figure 2.2: Sketch showing the electronics of the Crystal Ball. Into each MSCF-16 module (orange) channels of 16 PM-tubes (dark red) are connected. Their analog output is further processed and then sent to the trigger logics, while energy and timing signals go to ADCs and TDCs as respectively. Light blue shows an additional trigger signal used for off-spill muon triggering, the green (dashed) shows an update to be implemented soon.

S389) experiment. Then the signal is send from the MSCF to an ADC followed by data storage (if triggered).
The timing pulse is first filtered and then split one more time. One part is summed with the corresponding 15 signals from other PM-tubes and the sum sent to a leading-edge discriminator which, in case the signal is above threshold, sends a trigger to the local XB "trigger logic". The other part of the filtered timing pulse goes into a CFD which creates two output pulses, one goes through a delay to a TDC and the scaler unit, those two serving the data recording. Between the other pulse and the 15 corresponding ones a logical OR is created and send to the local XB "trigger logic".
The XB "trigger logic" consists of Fan-in/Fan-out modules create an OR between the outputs of the LEDs inside the MSCF's to give the "XB-sum trigger" and creating an OR between the the OR-outputs of the MSCF's to give the "XB-or trigger". The created triggers are sent to the global trigger unit. Another task performed by it was to create an OR of the outputs of all modules from each half of the XB and to then creating a logical AND of the two, which gave for S393 and S389 the "L+R muon trigger".
A problem with this system is that the timing of the sum trigger is due to the LED very energy dependent (walk). This will be solved by an upgrade, indicated in green (dashed) in Fig. 2.2. This will allow to sum all channels in an analog way and then send that signal to a CFD in order to get an energy independent timing of the sum trigger.

In the following is presented what has to be done in order to do a full calibration of the Crystal Ball and described which of these tasks have been done during this work and how. This comprises especially the efficiency calibration, for which several possibilities are presented and compared.

2.1 Calibration of the Crystal Ball detector

First a short overview about all calibration steps required for the Crystal Ball is given. The very basic calibrations are the energy calibration of the γ branch, the energy calibration of the proton branch and the timing calibration of the individual channels. Afterwards it is necessary to find an addback routine, do walk correction and perform an efficiency calibration. Addback needs to be done when the energy of one particle is

spread among more than one detector module. Identifying such events and ascribing the energy deposited to one position or track is called addback. Walk correction needs to be done when the timing of a trigger is dependent on the height of the signal. This is the fact for LEDs, those have a certain threshold and trigger when this is exceeded. A higher pulse rises steeper and thus triggers earlier compared to a lower pulse whose onset arrive at the same time. Correcting for this effect is possible after data collection as the walk is energy dependent. How to do this is explained e.g. in Ref. [13]. Except for the addback routine and the walk correction, the routines of each calibration are described in the following. Specifically in the S393 experiment there were problems with the BLR. When switched on the BLR created series of additional "events" without times (as they were created at the BLR). These "events" of one series were all in one crystal with decreasing energy after a non-noise energy deposit (for both cosmic and source runs) and series were seen in all crystals. Therefore, one also needs to find out what effect the BLR has in detail and find a way to eliminate that effect.
Generally the tools for unpacking and calibration of the RAW-data listmode files from experiments with the LAND-setup are collected in the program package *land02*. The in the following mentioned programs *gamma1* and *gamma2* belong to it. The program package and further information can be obtained from Ref. [9].

2.1.1 Methods of the basic calibrations performed

The energy calibration of the γ-branch is the first step towards a calibrated XB. This is performed using data from calibrated sources, preferably from before, during and after an experiment in order to check if the calibration parameters drifted during the experiment. A generally occurring problem is that sources provide only γ-energies up to 4 MeV, however the γ's emitted from reactions are usually of higher energy, up to several tens of MeV due to the Doppler boost at relativistic energies. Therefore, one is forced to calibrate the XB in the lower energy part of the γ-branch and assume that the linearity of scintillator, PM-tubes and modules is sufficient to allow an extrapolation towards higher energies. Performing the calibration one fits the calibration spectra obtained from the sources as shown in Fig. 2.3, i.e. a gaussian-shaped peak sitting on a linear background. Then one plots the obtained positions (in channels) versus the peak energies, and fits

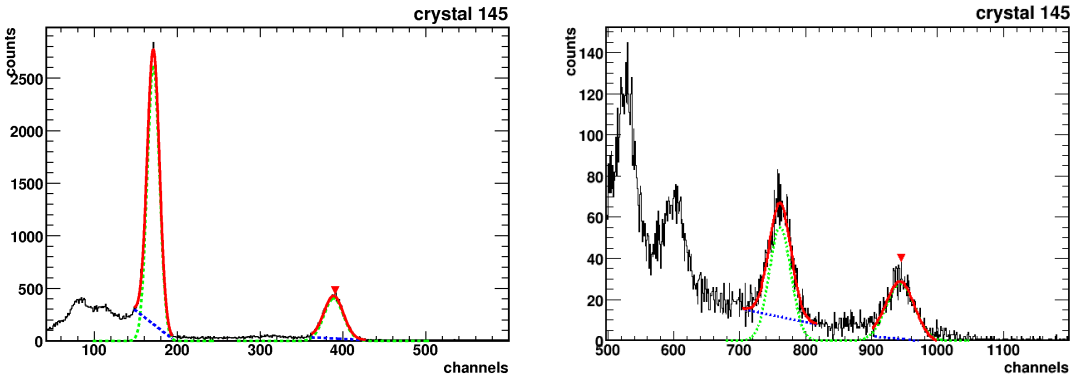

Figure 2.3: The plots show the fitting of spectra obtained from ^{22}Na (left) and ^{56}Co (right). The blue dashed line is the linear background fit, the green dashed line the gaussian peak without background and the red solid line represents the sum of background and (gaussian) peak.

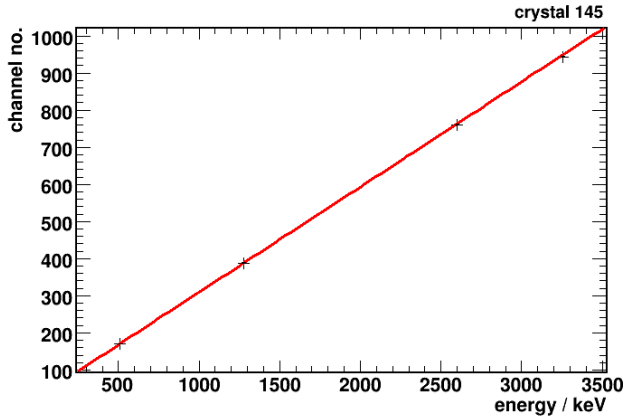

Figure 2.4: Plot showing the linear fit (red) of the data points (black crosses) obtained from fitting peaks in source spectra. The fitting routine takes errors into account. The errors are smaller than the symbol size and therefore hardly visible. For this plot ^{22}Na and ^{56}Co sources are used.

a linear function to these, taking into account the errors of the positions, as illustrated in Fig. 2.4. This results in the relation of energy versus channels; offset and slope are written to two calibration-files [14].

The next step is the timing calibration, which requires energy calibration-files. There are two calibration files to be created. The first one just gives the gain of each TDC for each crystal, this is usually known and can be written down directly. In order to find the different timing offsets between the crystals one can use a routine from *gamma2*, a program from the *land02*-package.
This routine also uses data collected using calibrated sources and is currently prepared for ^{22}Na, ^{60}Co and ^{88}Y data but can easily be adjusted for other sources. The offset determination is done as follows: the program sorts a raw data list-mode file and checks for each event whether the two expected γ-energies were detected in exactly two crystals with the sought-for energies. There is no energy-maximum imposed on the neighbour crystals, in order to avoid problems with noisy neighbour crystals. Random coincidences, though, are suppressed as much as possible by requiring exactly two crystals. The time difference between those two coincident events is saved in a histogram. For each crystal combination a histogram is filled. The thus collected data of time differences is fitted with a gaussian in order to obtain a mean time difference between all crystal combinations. These can be used to solve an equation system determining the offset of each crystal from the mean timing. In order to obtain a unique solution mean timing is set in a way that the sum of all offsets results in zero. Therefore, one has n = 162-(missing crystals) unknowns and at best $\frac{(n-1)n}{2}+1$ equations [15]. This is usually not the case as not all crystal pairs collect enough statistics to allow for fitting an average time difference. Solving the remaining equations produces an output that is saved into a calibration file.

The last basic calibration to be explained here is the proton-branch calibration of the 64 forward crystals with proton read-out. This is done using cosmic muons. The program *gamma2* allows to sort the data with two further options which can be used for the proton-branch calibration. One option selects events which are supposed to be muons traversing the crystal ball through two (almost) opposite crystals, “opposites”, while the other option aims at extracting events where muons have traversed a chain of crystals, “grazing”. These two options of traversing the XB are illustrated in Fig. 2.5. Opposites

are muon paths like 4 and 5 shown in Fig. 2.5 and gracing are paths 1 to 3, but only path 3 fulfills all requirements, as described in the following. In order to classify an event as a potential muon event in the offspill[1)] data, the energy in the γ-branch has to exceed 5 MeV (high energy deposit) , events exceeding the ADC range (overflows) are also used.

In order to find "opposites" the routine sorts all high-energy deposition events and checks whether the opposite (like in path 5 of Fig. 2.5) or a neighbour (up to the next-neighbour level) of the opposite (like in path 4 of Fig. 2.5) has also detected an energy above threshold (i.e. larger than 0.5 MeV, noise-threshold). If one or two crystals fulfill this condition, the event is treated further, while all other events are discarded. If two opposite crystals were found, they have to be neighbours in order to allow this event to be treated further[2)]. Finally for the event to classify as an opposite traversing, the neighbours of the crystal with the high-energy deposition (recall: larger than 5 MeV) are checked and if the signal of those did not exceed noise-threshold, the event is stored for this crystal. There are several parameters saved for such an event: the crystal number (c), the energy of the crystal in proton and γ-branch in channels (re1, re0), if there was a calibration file also in energy units (se1, se0), the time difference (dt), and an index being a measure for the deviation

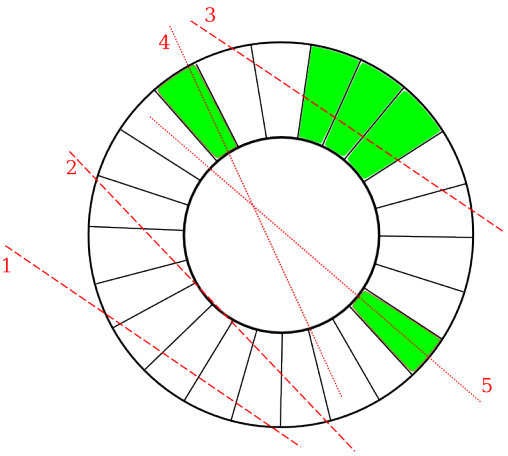

Figure 2.5: Sketch showing schematically how muons might traverse the XB. Paths 1, 2 and 3 indicate potential "grazing" muons, while 4 and 5 indicate "opposite" muons. Green crystals mark the ones data is stored for. For details see the text.

[1] The beam of nuclei arriving at the experiment is bunched, i.e. not a continuous stream of particles but chopped up into intervals where there are nuclei and where there are not, this is due to the acceleration technique. When ions arrive at the experiments (which are detected by the beam tracking detectors) one calls this inspill. When there are, due to these empty intervals, no ions arriving at the experiment, but a (or several) detector(s) record data this is called offspill. One also refers to offspill data when there was no beam supposed to arrive at the experiment but data was collected for e.g. calibration purposes.

[2] As then only information for the crystal which was on the other side of the two neighbours is stored one does not need to be so strict forcing the opposite to be in only one crystal.

between the "opposite" firing and the physically opposite crystal (r). The index r is calculated by summing the distance of the one or two opposites from the real opposite crystal[3)] and dividing by the amount of opposites found (1 or 2).
In order to sort the "grazing" events, *gamma2* first sorts the crystals for each event into three groups, those which detected a high energy deposit (>5 MeV and overflows) in the γ-branch, those which detected something above noise-threshold, and those which did not detect something above noise-threshold. Then it loops over the crystals which had a high energy deposit and tries to find a neighbour which had an energy above noise-threshold. If one is found and the common neighbours of such a pair are clean, i.e. did not detect something above noise-threshold, the event is kept. After all crystals are paired up *gamma2* tries to match the pairs together in order to form chains of crystals, with a length of five to eight crystals[4)]. Because the common neighbours of all pairs are required to be clean, the outcoming chains are almost straight and their surrounding neighbours are all clean. One unwanted case which is possible with these restrictions is "forking" of a chain at a hexagonal crystal, i.e. the chain splitting up to have 3 ends instead of two. These chains are sorted out and all pairs belonging to it discarded.
The resulting chains are stored into a ROOT-tree [16], data is stored for all crystals of a chain except the outer two of each chain end. The information stored are crystal number, energy deposit (for both γ- and proton branch, both raw and calibrated if there was an energy calibration), the length of the chain, the distance of the crystal to the center of the chain and an index shp2 providing information on which crystal shape was traversed in which way. Each shape is assigned a value, i.e. A=0, B=1, C=2, D=3. The index is then calculated in the following way:

$$shp2 = 16 \cdot s + 4 \cdot s1 + s2 + o \cdot 64 \tag{2.1}$$

where s is the value of the shape of the crystal for which data is stored, $s1$ the value of the shape of its chain-neighbour with the lowest shape value and $s2$ the value of the shape of the other chain-neighbour. The parameter "o" indicates of the two chain-neighbours of the crystal lie completely opposite ($o = 0$) or not ($o = 1$). This is necessary in order

[3] This means 0 for a real opposite, 1 for a neighbour of the real opposite and 2 for next-neighbour.
[4] For shorter chains (like path 1) the path through the central crystal(s) of the chain is not well defined and for longer chains (like path 2) the muons are not very likely to travel completely through the central crystal(s) but also through the inner sphere of the XB, so their path is also not well defined, see Fig. 2.5.

to correctly define the pathlength of the muon in each crystal.
The energies for the different transitions are obtained by simulations of muons traversing the XB. So far only a preliminary simulation for opposite traversing muons exists[5]. How to do a more elaborate and accurate simulation is described in section 2.3.

2.1.2 Documentation of basic calibrations

For the present experiment, S393, data taken with ^{22}Na, ^{56}Co and ^{60}Co were available for calibration. The energy calibration of the γ-branch was performed with data from ^{22}Na and ^{56}Co, providing an equidistant distribution of points for the linear fit as can be seen in Fig. 2.4. A calibration based only on ^{22}Na and ^{60}Co is not reliable and deviates visibly beyond 2.5 MeV. Calibration data for those two sources was only taken in order to provide information on the drift of the calibration parameters during the experiment see Fig. 2.6, as data from ^{56}Co was only taken once after the experiment. Using data from all three sources for the linear fit does not work either as the ^{60}Co γ energies lie very close to each other around the higher ^{22}Na γ-energy (1.275 MeV)[6] and thus the calibration is essentially governed by those three points, and gives usually a too large slope, as shown in Fig. 2.7. Nonlinearity was excluded to be causing this deviation of the slope, because of the nonsystematic under-/overestimation of the slope but more powerful by Ref. [17] stating the integral nonlinearity of the module (MSCF-16) to be less than 0.05%. A nonlinearity in the crystals and corresponding PM-tubes would still be possible, but is unlikely at these energies.
A very preliminary proton branch calibration was performed using the energy deposit obtained from first-attempt simulations by R. Reifarth for muons traversing two opposite crystals in the XB. A time calibration was also performed according to the description above.

[5] Done by R. Reifarth.
[6] The 511 keV γ's stem from the annihilation of the emitted positron.

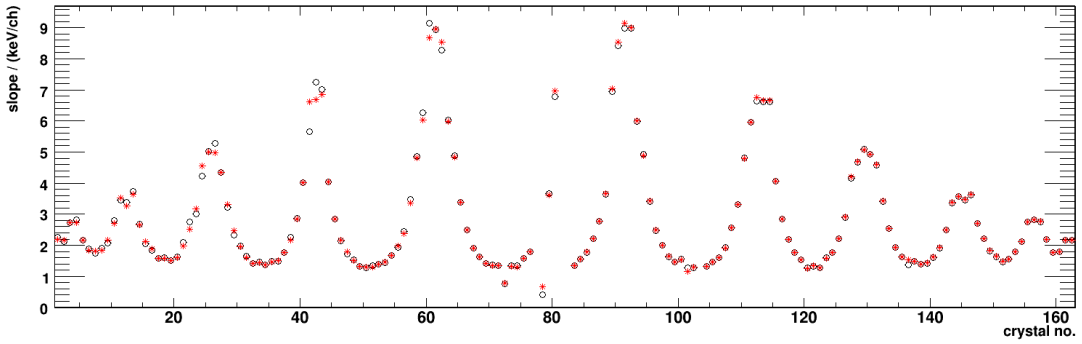

Figure 2.6: This plot illustrates which crystals drifted over the course of the experiment. The obtained slope (keV/ch) is plotted versus the crystal number, (black) circles show calibration parameters at the beginning of the experiment and (red) stars show the calibration parameters from the end of the experiment. The error bars are about the size of the symbols. Several crystals, e.g. numbers 22,41,59,62 and 78 drift by values exceeding the errors of the calibrations.

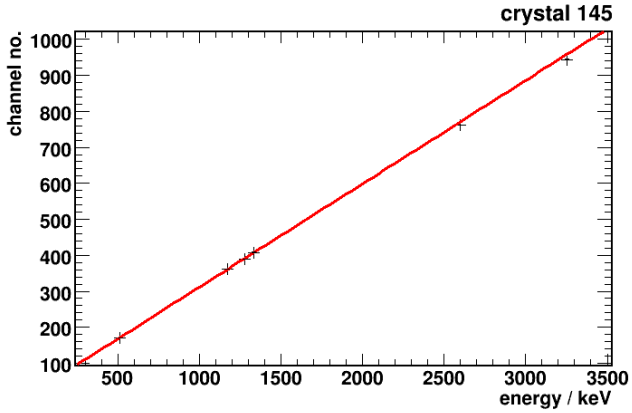

Figure 2.7: Plot showing the linear interpolation of data points obtained from all available sources. It can clearly be seen that the three close points due to lines in ^{60}Co and ^{22}Na govern the fit, resulting in a significant deviation of the fit from data points obtained with a ^{56}Co source already at 2.5 MeV.

2.2 The efficiency calibration of the XB

In general the fraction of radiation or particles at a given energy where the total energy amount emitted is detected is called the total photo-peak efficiency of the detector. It depends on geometry, dead-time, material in the path between detector and source and on the intrinsic efficiency. The latter is a pure detector property, being a measure on how many particles that impinge on the detector with a certain energy are fully detected. As one can correct for dead-time and geometry in a straightforward fashion, the intrinsic efficiency together with the material between source and detector are considered in the following.
It is necessary to perform an efficiency calibration in order to be able to deduce absolute numbers from the measured data. As no detector is perfect (i.e. detecting all particles) a certain fraction of events is always lost and this has to be determined.
Specifically efficiency calibration is also necessary in order to avoid skewing of results by different efficiencies of different detectors or detector parts. In order to determine e.g. absolute cross-sections this is important. Thus for the XB one needs to know the efficiency of each crystal. The efficiency calibration is one of the "advanced" calibrations to be done for the XB. In this work three different methods to perform such a calibration were tested and their results are compared. First all methods are introduced, afterwards the corresponding results are presented and discussed.

2.2.1 The three different methods of efficiency calibration

The first method has been used previously to determine the efficiency of the XB in Ref. [12] where it was employed using an ^{88}Y source. It needs data from a calibration source, whose decay features the emission of two successive γ-rays in the following referred to as γ_A and γ_B. The procedure of the first method, called counting method in the following, is based on the number of counts detected for γ_A and γ_B. If more than one of each γ-energies was recorded during one event, the event is disregarded in order to suppress random coincidences. If one γ_A was recorded, the total γ_A count, A_{tot}, is raised by one. If (under the condition that one γ_A was recorded) also a γ_B was observed the count for

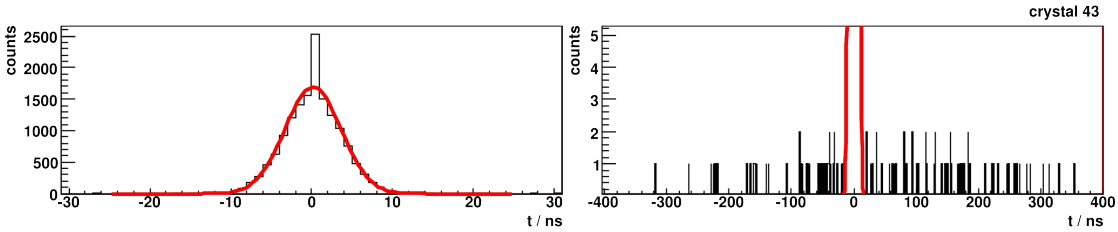

Figure 2.8: Plots illustrating the time difference between trigger-γ and the one registered in crystal 43, on two different scales. Note these are identical plots differently scaled. Left: the whole peak is visible 3σ are at about 11 ns, right: zooming in on the y-scale and zooming out on the x-scale (with respect to the left plot) shows that there are additional random coincidences.

γ_B of the crystal n which saw γ_B, B_n, is raised by one, and vice versa. In this way one obtains for each crystal an amount of γ_A, A_n and an amount of γ_B, B_n detected under the condition that also the respective other γ was detected and the total amount of γ_A, A_{tot} , respectively γ_B, B_{tot}, detected. In order to suppress random coincidences an additional constraint on the time difference between those two registered γ's was introduced: the two gammas are allowed to be maximum 12 ns apart (in time). This includes all real coincidences as illustrated in Fig. 2.8, but excludes most of the (few) randoms.
Basically the efficiency, ϵ of crystal n is determined by calculating:
at energy of γ_A: $\epsilon_A \propto \frac{A_n}{B_{tot}}$
at energy of γ_B: $\epsilon_B \propto \frac{B_n}{A_{tot}}$
It is necessary to correct for the geometry by dividing the total counts by 162 (as each crystal covers a solid angle of $\frac{1}{162}$ of a sphere), and to correct for possible different emission probabilities of the two γ's. This gives the intrinsic efficiency (together with effects from the material in the path) of each crystal at two different energies:

$$\epsilon_A(crystal\ n) = \frac{A_n \cdot 162}{B_{tot}} \cdot \frac{a_B}{a_A} \qquad \epsilon_B(crystal\ n) = \frac{B_n \cdot 162}{A_{tot}} \cdot \frac{a_A}{a_B} \quad (2.2)$$

with a_A and a_B being the relative intensities of γ_A and γ_B respectively.
In this work the intervals in which the peaks were counted were obtained from peak positions and variances (σ) obtained from a previous fit of the same spectrum[7)]. The

[7]The fit function was a sum of two gaussian peaks on a linear background.

intervals were chosen to be one σ on the side of the peaks close to the other peak and to be 2σ on the side of the peaks pointing away from the other peak. This had to be done in order to avoid overlapping of intervals because the two γ-energies of the used ^{60}Co source are very close with respect to the energy resolution of the NaI crystals.

Method number two, in the following the sum peak method, is used for calibrating similar detectors like the Miniball [18] and the Euroball [19] and described for example in [20]. It also requires a source which emits two successive γ-rays, and good statistics. In order to use this method one needs to obtain spectra from the calibration runs in which the sum peak of the two γ-rays contains enough statistics to be fitted above the present background. Fitting of the sum peak as well as of the two individual peaks is realized similar to the fitting procedure described for the energy calibration of the γ-branch (see Sec. 2.1.1). The major differences are that energy- and time-calibrated spectra are used which facilitates peak finding and that an average peak-to-noise ratio is calculated before fitting the sum peak. The sum peak is not fitted if not exceeding the statistical fluctuations of the background. Another difference is in the background fitting routine. It was changed such that the first estimate fit of the background was only defined outside the peak regions around the peak in order to avoid overestimation of the background due to the peak. For the fit of the combination of gaussian(s) on linear background the thus obtained linear function is taken as starting point for the linear part.
From the fit of peaks on background the areas under the peaks (without background) are known. Dividing the sum peak area by the area of a single peak results in the efficiency of the corresponding other peak. In order to obtain the intrinsic efficiency corrections are necessary. The geometry factor of $\frac{1}{162}$ needs to be used (for different reasons as before because here one requires for the sum peak that two γ's hit the same detector with the solid angle of $\frac{1}{162}$ of a full sphere, while for the single peaks one requires only that one γ hits the detector with solid angle $\frac{1}{162}$). The second correction has to be done due to the directional correlation of two successive γ-de-excitations of a given multipolarity. In this work only one calibration set using a ^{60}Co source had sufficient statistics to be employed for this method. Therefore, the correlation of the two γ-rays at 1332.5 keV and 1173,2 keV from this source is described in the following. For a detailed description of angular correlation of γ-rays see Ref. [21]. In Ref. [22] the directional correlation function $W(\theta)$,

describing the relative probability that the second γ is emitted at an angle θ with respect to the first, is presented together with coefficients for different transition multipolarities. The γ's emitted after β-decay of the isotope ^{60}Co belong to a 4-2-0 transition[8)][23] and the coefficients from Ref. [22] lead to the correlation function:

$$W(\theta) = 1 + \frac{1}{8}\cos^2(\theta) + \frac{1}{24}\cos^4(\theta) \tag{2.3}$$

The crystals each cover a solid angle of $\frac{1}{162}$ of a sphere, by approximating their shape by a circle, one can calculate the corresponding opening angle to be $\theta_{\max} = \tan^{-1}(\frac{\sqrt{2}}{9})$. In this manner, all γ's emitted at angles between zero and $\theta_{\max}$ from the preceding γ can contribute to the sum peak. The correction factor is then obtained by taking the ratio of the integrals S and A:

$$S = \int_{\theta=0,\phi=0}^{\theta=\pi,\phi=2\pi} W(\theta) d\cos(\theta) d\phi \tag{2.4}$$

$$A = \int_{\theta=0,\phi=0}^{\theta=\theta_{\max},\phi=2\pi} W(\theta) d\cos(\theta) d\phi \tag{2.5}$$

this gives the correction factor $c = \frac{S}{A}$ for the directional correlation already including the geometrical factor $\frac{1}{162}$ argued for earlier. If the source used has different relative intensities for the two γ's, because one of them belongs also to another de-excitation-route, one has to correct for that as well. For ^{60}Co the relative intensities are almost the same, being 99.9736 % and 99.9856 % for lower and higher energy peak respectively.

The third method employs a measurement, in which only one crystal PMT at a time was biased for 5 seconds, each. From the scaler information stored one can retrieve the exact event-number interval and corresponding time during which a crystal was collecting data alone[9)]. Subsequently, one extracts the spectrum of the crystal taken during that interval and fits the two peaks. Ideally the fit is done with gaussians on a linear background. From the area under the peak, the intrinsic efficiency can be calculated in

[8] The numbers describe the nuclear angular momentum.
[9] This is important in order to take deadtime correctly into account.

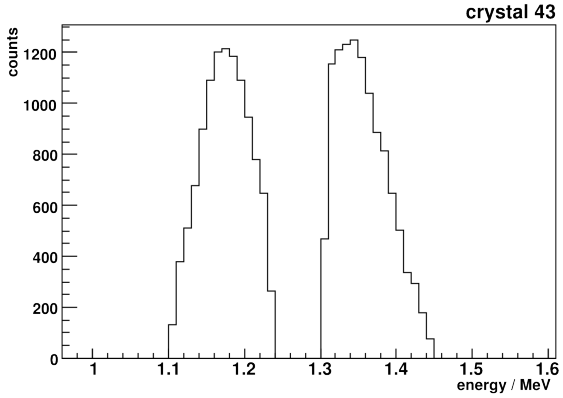

Figure 2.9: Plot of the energy distribution of the events which were counted for crystal no. 43 with the counting method. Note the cutoffs are due to the ranges set. The ranges do not correspond to bin boundaries in the histogram, thus the cutoffs are not sharp.

the following way:

$$\epsilon = \frac{A \cdot 162}{a \cdot \Delta t \cdot f \cdot c} \tag{2.6}$$

with A the area of the fitted peak, a the activity of the source, Δt the time interval data was taken in, and f the fraction of accepted trigger vs. total triggers. In this work, the statistics is unfortunately insufficient for fitting the entire spectrum. Only two gaussian peaks but no background could be fitted. This is definitely not ideal, and in order to be able to use this method reliably, it is necessary to obtain higher statistics.

2.2.2 Results of the efficiency calibrations

For the counting method, described in section 2.2.1, the energy of counted events for one example crystal is shown in Fig. 2.9. Recalling that the spectrum was cut at 2σ on the side pointing away from the neighboring peak and at 1σ on the side towards the neighboring peak, this explains the observed distribution. No sharp cutoffs are seen as the range-limits do not correspond to certain bin terminations.
The results from employing this calibration method are shown in Fig. 2.10. It can be seen that the curves for the two different peaks are quite similar. The escape of the efficiency of crystal no. 101 for the 2^{nd} peak can be explained by a very large value of

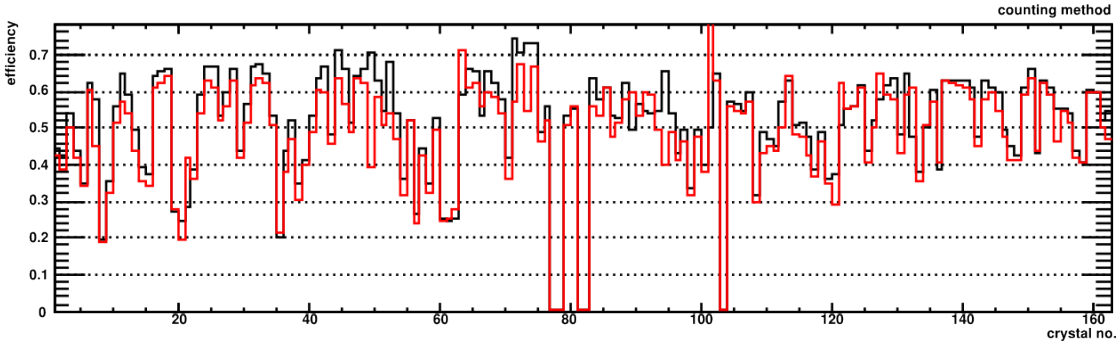

Figure 2.10: Plot showing the efficiency of each crystal obtained from the counting method with the peaks of ^{60}Co at an energy of 1.176 MeV (black), and at an energy of 1.333 MeV (red). No error bars are shown as no error could be calculated as explained in the text. Crystals 78 and 103 are due to their bad resolution excluded from this method.

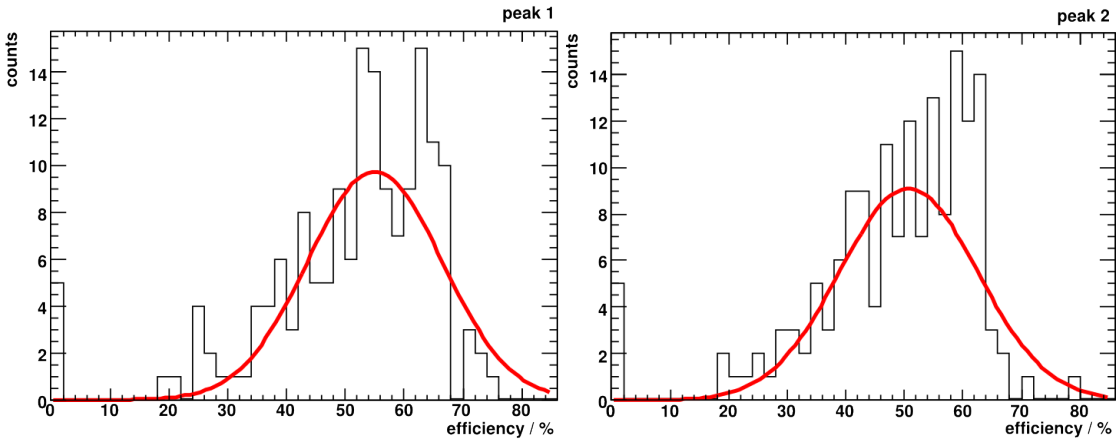

Figure 2.11: Plot showing the distribution of calculated efficiencies (black) by the counting method for peak1 (left, energy of 1.176 MeV) and peak2 (right, energy of 1.333 MeV). The red curves are the fitted gaussian distributions, which were fitted in the displayed regions excluding the (0-2)% bins. For resulting averages and widths see text.

the σ which leads to a large window. This results in a very high number of counts due to contributions from the region of the lower-energy peak. It is expected that the efficiency for the peak at higher energy is lower, however this is not the case for 15 crystals with that method. The average efficiency of the detectors at peak1 and peak2, respectively, are obtained from fitting gaussians to the distributions shown in Fig. 2.11. This results in average efficiencies of (55.1±1.1)% and (50.7±1.2)% and in σ's of (11.4±1.1)% and (11.8±1.2)% respectively. This is, as expected, a lower efficiency for the higher energy peak, but the same width.
For this method it was, however, not possible to estimate the error in a reasonable way because of the large amount of input parameters, interacting in a nontrivial way. In particular, the input parameters of peak position and sigma of the two peaks for each crystal spectrum are correlated as they are fitted as a sum of two gaussians. The influence that a variation of peak position or sigma has on the number of counts detected in total and on the number of counts seen by one crystal, cannot be described by a simple function. This causes, however, the largest part of the uncertainty, the statistical error of less than 1% being negligible in comparison[10)].

The sum-peak method used a fit of the spectrum in order to obtain the areas under the peaks and the sum peak in order to calculate the efficiency from the areas, as explained in section 2.2.1. An example of such a fit of the spectrum is presented in Fig. 2.12.
The results of the efficiency calibration performed according to this method are presented in Fig. 2.13. The criterion that the efficiency for the second peak has to be smaller than that for the first peak is not fulfilled in seven instances, four of which do not have a sum peak visible above background. The widths of the determined efficiencies are obtained by fitting a gaussian to the distribution of efficiencies shown in Fig. 2.14 and resulted in σ's of (8.13±0.76)% and (7.57±0.55)% for the lower and higher energy peak, respectively. The average efficiencies obtained from the fit are (36.44±0.77)% and (34.65±0.65)% for first and second peak respectively.
The errors of the spectrum fit (see Fig. 2.12) are propagated in order to obtain the error of the determined efficiency, and are displayed in Fig. 2.13.

[10] Changing the peak position with the given error from the fit amounted to a change in the efficiency of about 5% in the respective crystal.

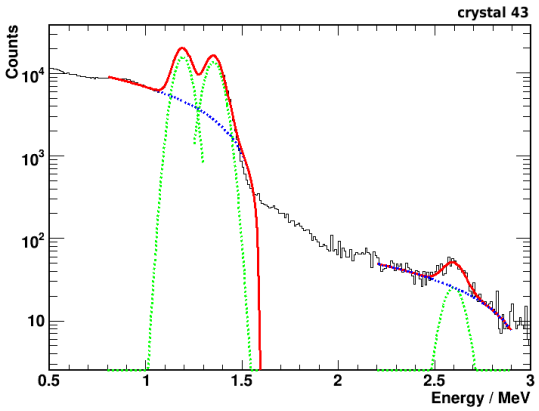

Figure 2.12: Example plot illustrating the fitting of the sum-peak method, the spectrum is from crystal no. 43. Blue dotted lines are background fits, green dotted represent the gaussians and red the sum of gaussian(s) and background. The two single peaks are fitted with a common background and as a sum of two gaussians.

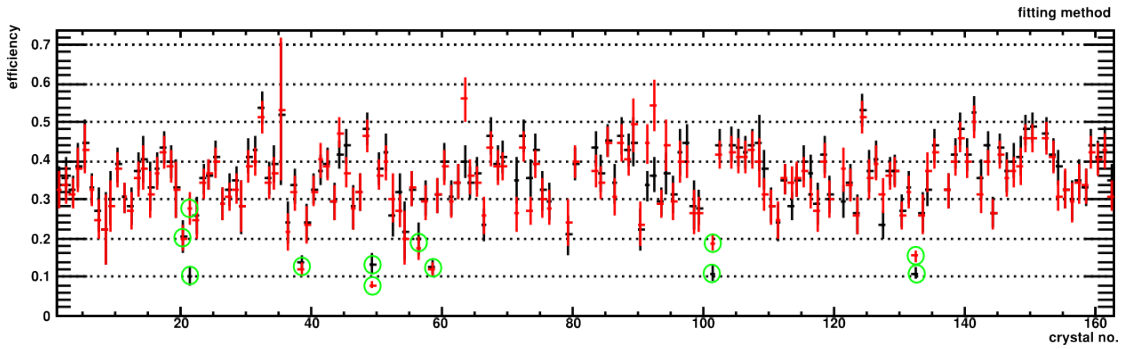

Figure 2.13: Plot showing the efficiency of each crystal obtained from the sum-peak method with the peaks of ^{60}Co at an energy of 1.176 MeV (black), and at an energy of 1.333 MeV (red). The green circles mark results obtained as upper limit, for crystals for which the sum peak did not exceed the statistical variation of the background. Some crystals are missing, due to poor-quality spectra.

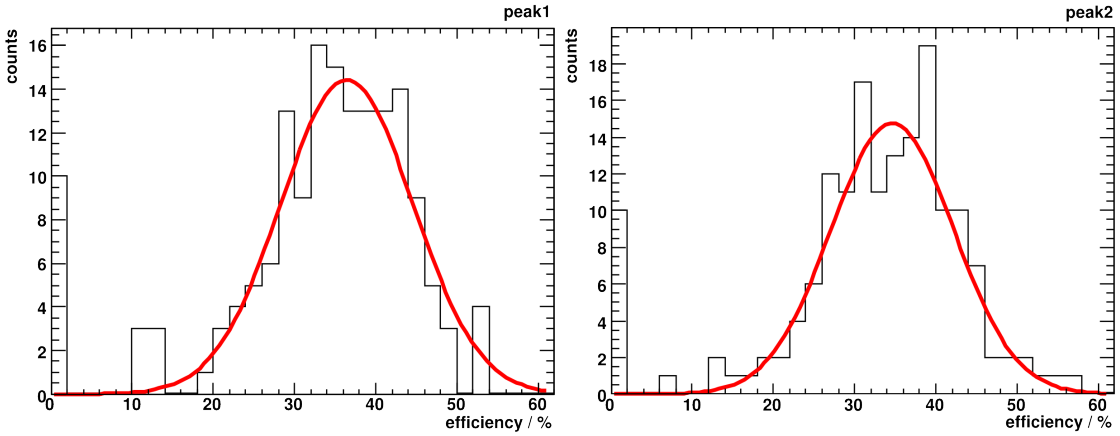

Figure 2.14: Plot showing the distribution of calculated efficiencies (black) by the sum-peak method for peak1 (left, energy of 1.176 MeV) and peak2 (right, energy of 1.333 MeV). The red curves are the fitted gaussian distributions, which were fitted in the displayed regions excluding the (0-2)% bins. For resulting averages and widths see text.

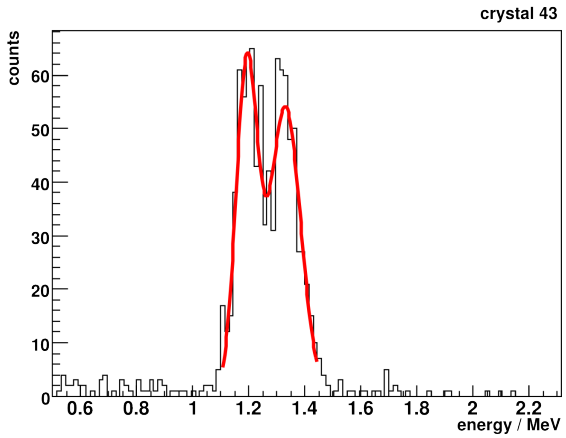

Figure 2.15: Plot displaying the spectrum obtained for crystal 43 during 2 seconds of the time it singly was switched on. The spectrum is interpolated with a sum of two gaussians seen as the red curve.

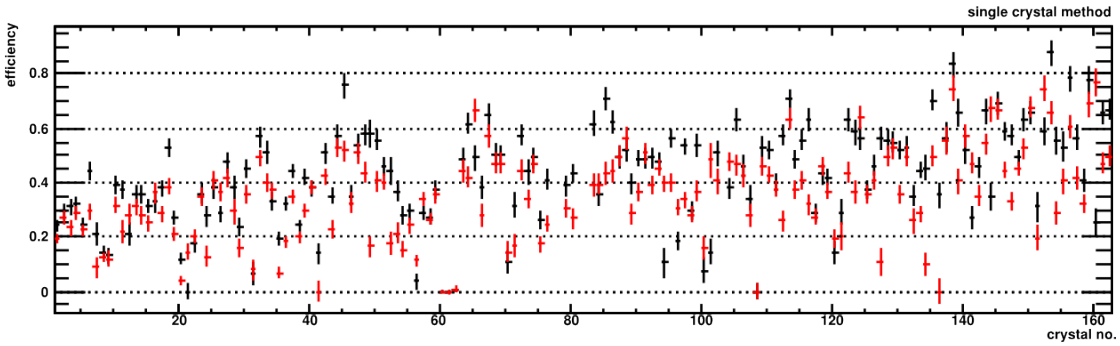

Figure 2.16: Plot showing the efficiency of each crystal obtained from the single crystal method with the peaks of ^{60}Co at an energy of 1.176 MeV (black), and at an energy of 1.333 MeV (red).

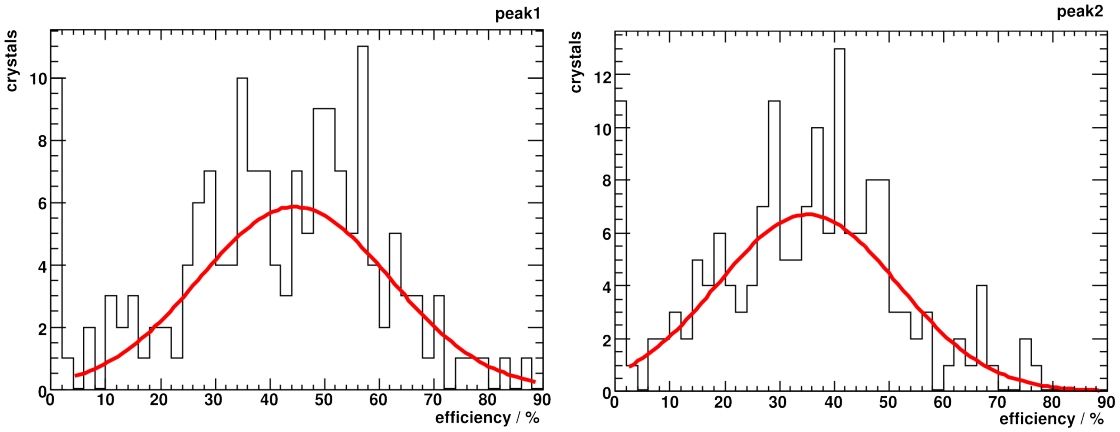

Figure 2.17: Plot showing the distribution of calculated efficiencies (black) by the single crystal method for peak1 (left, energy of 1.176 MeV) and peak2 (right, energy of 1.333 MeV). The red curves are the fitted gaussian distributions, which were fitted in the displayed regions excluding the (0-2)% bins. For resulting averages and widths see text.

The single crystal method interpolates simply the spectrum obtained in the 2-4 seconds a crystal PMT was biased alone and calculates the efficiency from time and activity of the source, as explained in detail in section 2.2.1. In Fig. 2.15 an example of such a spectrum is shown. It is evident that the statistics is not very good, but that the background seems negligible. The results of this method are displayed in Fig. 2.16. As can be seen only seven crystals do not fulfill the expectation of a lower efficiency at higher energies, but the values fluctuate strongly, especially for large crystal numbers to values which exceed the theoretical limit. The vanishing efficiency for crystals 60, 61 and 62 is due to the fact that the gain of their PMT is so small[11)] that the signals do not trigger the CBsum trigger (TPAT9) but only the CBor trigger (TPAT12), see Sec. 2. For all others though, the CBsum trigger had to be used as the CBor trigger only triggered on lower energies. That was probably due to the fact that the CBsum trigger is so early that the CBor comes after the gate and is thus not registered.
The strongly fluctuating values are also represented by the width, the σ of the gaussian fitted to the distribution of efficiencies, shown in Fig. 2.17, resulting in (17.8±2.0)% and (16.5±1.8)%, by far the largest width of the three methods. The mean for the peak positions respectively obtained from the gaussian fit are (44.4±1.8)% and (35.2±1.7)%.

2.2.3 Discussion of the results obtained from the three different methods

One expects that the three different methods would give, within error bars, the same efficiency. This is not the case as shown in Fig. 2.18 (though errorbars are not shown here for improved clarity, c.f. errorbars are given in section 2.2.2). There exists one region, though, where the sum-peak and the counting method have rather good agreement, for crystals 36 to 46 namely the results of the two methods only differ by an offset. It should also be noticed that major escapees are correlated with unfulfilled expectation of lower efficiency at higher energies in one or more methods. This is the case for crystal numbers 21, 35 49, 62, 63, 65, 66, 89, 91, 92, 94, 95, 101, 104, 113, 126, 132, 142, 144 and 160. It also seems to be the case that for the right half (crystals 1 to 81) the three methods agree better than for the left half (crystals 82 to 162), there are also less broken self-correlations (only seven). Especially the single crystal method produces

[11] They are in the most forward direction, thus the particles impinging have high energy and the gain needs to be lower in order to avoid overflows.

doubtful results for the left half, but also the sum-peak method has more fitting problems. Generally only the sum-peak method does not produce efficiencies higher than the theoretical maximum. This is also reflected by the averages, the sum-peak method having the lowest average with (34.65±0.65)% while the counting and the single crystal method have (50.7±1.2)% and (35.2±1.7)% efficiency, respectively, for peak two[12)].
The single crystals method seems to be the least reliable. This is probably due to poor statistics as can be seen in Fig. 2.15. Experimental limitations lead to the fact that not all 5 seconds can be used but only 2 to 4 seconds can be used. This is mainly due to the fact that it is necessary to determine the interval (in time and event number) in which the PMT of the specific crystal was solely biased, a consequence of that it takes time to ramp up and down the PM-tubes. This then has to be matched with a timestamp of the scaler, leading to an additional time-loss. For the present statistics this method is regarded as unreliable and will not be discussed further. In general though this method seems to be a very good idea, but needs longer time intervals in order to increase statistics.
A more disturbing question is the origin of the large discrepancies between the sum-peak and the counting method. The general offset between the two methods is probably due to the fact that it is not possible to account for the random coincidences in the counting method and that the background around the sum peak is quite noisy and the fitting routine might be overestimating the background due to that.
Comparing the results of the two methods with the result of an efficiency calibration of the XB for an older experiment by F. Wamers [12] with data from a ^{88}Y source, shown in Fig. 2.19 one can see that the result from the counting method in this work is very similar to the older calibration done with the same method. For some crystals the results differ, especially those which do not satisfy lower efficiency for higher energy, but the dips in efficiency are reproduced. According to Ref. [12] these dips are due to the material inside of the XB, namely, the target wheel, the holder of the same and the SSD mounting construction. The material thus explains the different results of the different methods as explained in the following.
A crystal with material between it and the source detects a smaller amount of γ's compared to if there was no material, because the material absorbs a certain fraction (depending on material and thickness). The problem occurring with the counting method is

[12]This excludes crystals which were excluded / are displayed with zero efficiency in Fig. 2.18

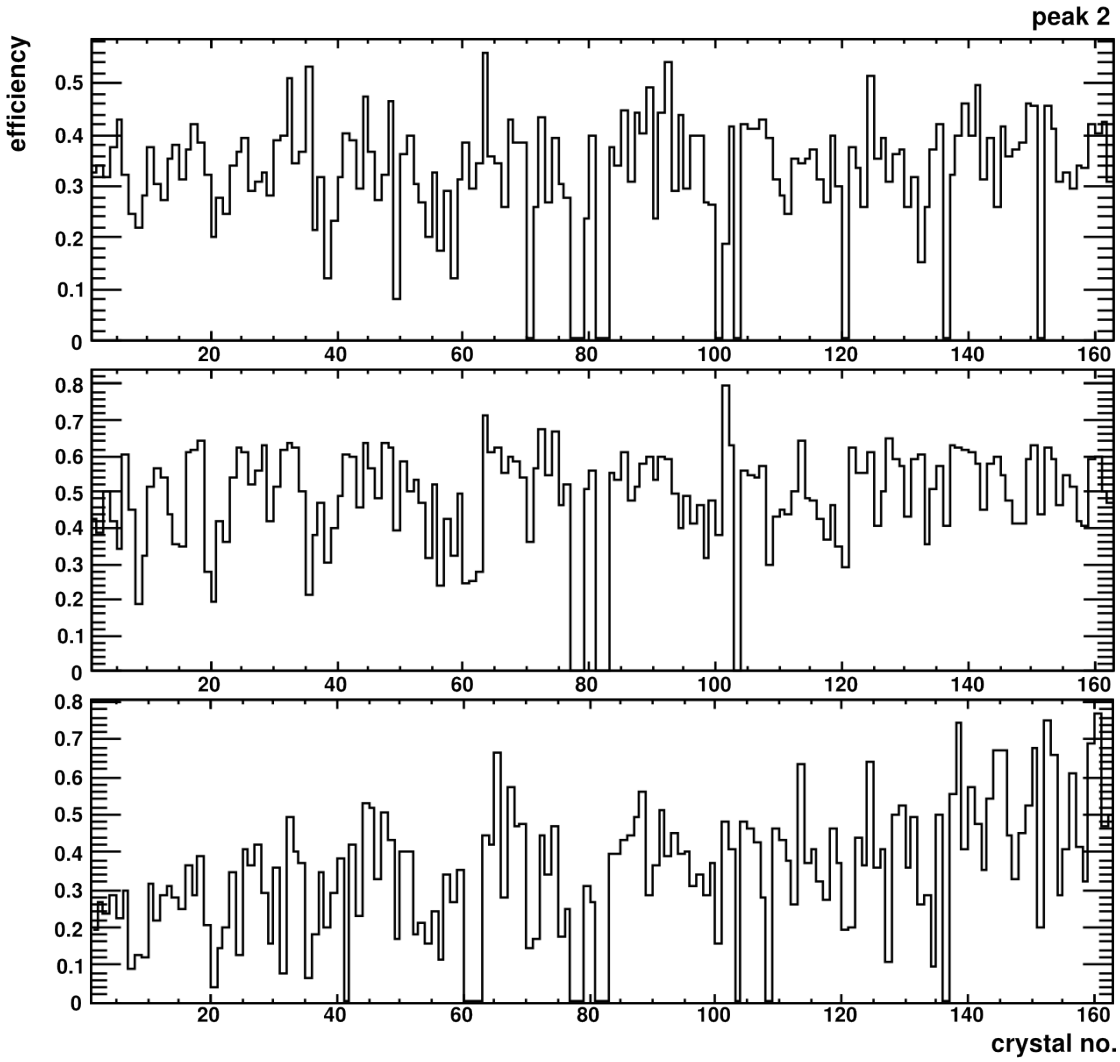

Figure 2.18: Plots of the efficiency obtained from the three methods sum-peak, counting, single crystals (top to bottom) for peak two (energy of 1.333 MeV). Some efficiencies from the sum-peak method are displayed as 0 % as fitting was not possible with in those cases. Crystal no. 103 has 0 % efficiency for all three methods because it was excluded due to bad resolution.

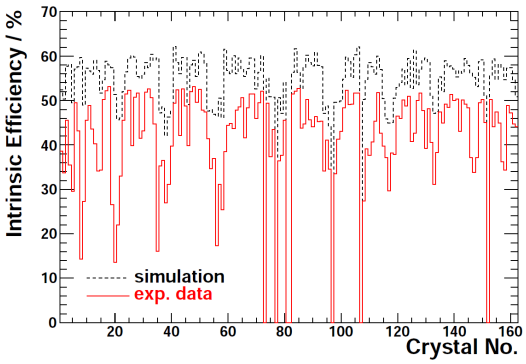

Figure 2.19: Plot of the results of the efficiency calibration (solid red curve) of the XB done with the counting method on the 898 keV peak of an ^{88}Y spectrum, done by F. Wamers in Ref. [12]. Additionally results of a simulation are displayed (dashed black curve) for details see Ref. [12].

that the total amounts of $\gamma_{1/2}$'s detected is taken to normalize the amount of $\gamma_{2/1}$'s seen by a single crystal (after triggering from $\gamma_{1/2}$'s from any other). These normalization counts are decreased by the material between any detector and the source, and therefore the efficiency is artificially increased for all crystals. Angular correlations worsen this, as the effect is not the same for all crystals.

The sum-peak method, however, does not have problems with this effect as one normalizes the amount of both γ's arriving at one crystal with the amount of single γ's (of a specific energy) arriving at the crystal. Thus if a certain percentage of γ's is absorbed due to material in the path, this is taken properly into account for by this method. If one regards that only a fraction f of the γ's penetrates the material then the square of this factor multiplies with the number of counts in the sum peak (once for each single γ which is needed to arrive at the detector) and once for each single peak. Thus the efficiency of the respective crystal is diminished by the factor f. So this method accounts for the material between source and detector, which will then also be between reaction and detector in the experiments and is not skewed. One could argue that γ-rays with different energies are absorbed differently. According to calculations done using Ref. [24] these absorption for a γ of 1.173 MeV is 0.32 percentage points higher than for a γ at 1.332 MeV[13]. The difference between the two γ-rays of ^{88}Y whose absorption differs by

[13]These were the energies used in this work from a ^{60}Co source.

1.8 percentage points, is not insignificant but still small and could easily be taken into account.
The single crystal method takes this absorption problem properly into account for obvious reasons.
Concluding, two methods, the sum-peak and the single crystal method, are capable of determining the intrinsic efficiency folded with the absorption which happens from target to crystal. The other method, the counting method, produces skewed results, as soon as material is between some crystals and the source/target and is therefore not recommended. Concerning S393 (and S389) the single crystal method is not reliable either, as the statistics is quite poor. This leaves the sum-peak method to be used as final result for S393. For future experiments one should use the single crystal method with better statistics.

2.3 Future prospects: muon simulation

As described in section 2.1.1 the proton branch can be calibrated with cosmic muons. So far, only a preliminary simulation for opposite traversing muons has been done and one can not be sure that the outcome is correct. Nevertheless the analysis tools are already there and thus it is shown in the following what is possible, and it is underlined why a copious simulation is necessary.

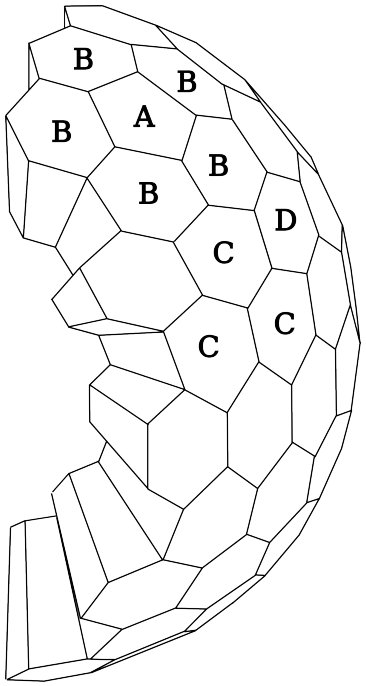

Figure 2.20: Sketch of a part of the Crystal Ball to illustrate different crystal shapes and positions. For a sketch of the full XB see Fig. 2.1.

Taking the cosmic muon data (i.e. offspill data) from throughout the experiment one can see that the energy deposited by grazing muons in a crystal depends on shape and position of the latter. First of all the deposited energy is dependent on the length of the chain of crystals the muon traverses, as shown for all crystal shapes in Fig. 2.21. Plots for all crystals can be found in A.1 . The shifts are due to different pathlengths through the crystals for the different chain lengths. The shifts may not be large, but in effect, if one does not single them out, they broaden the peak structure. Therefore constraining the chain length to six and seven crystals, seems sensible in order to study other effects. Later on one can include these chains and just take the shifts into account. As can be seen (in A.1) the different intensities for different lengths change systematically for most crystals, though some (which lie e.g. directly beneath the beampipe) have a different dependence due to the influence of geometry.

Other factors influencing the energy deposit of grazing muons are the position and shape of the crystal, resulting in different pathlengths inside a crystal, as already mentioned. The direction in which muons traverse a specific shape governs the energy deposit. This is illustrated in Fig. 2.22 where different energy deposits are shown for muons traversing

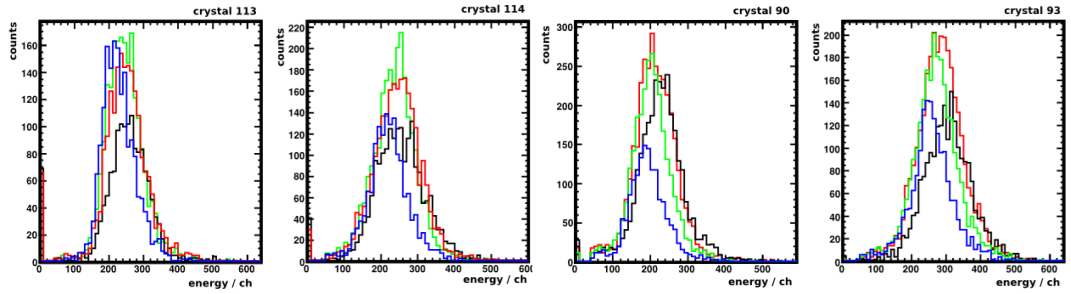

Figure 2.21: Four examples of different energy deposit due to differing pathlength are shown. The crystals are of shape A, B, C and D from left to right. The colors indicate the length of the chain considered, thus black corresponds to five crystals, red to six, green to seven and blue to eight. One can see that chains of length six and seven give similar output while the shorter and longer chains are shifted to lower or higher energies respectively. Those chains usually also show less counts, though not always as seen for crystal 113, where length eight has about as many counts as the chains of length six or seven.

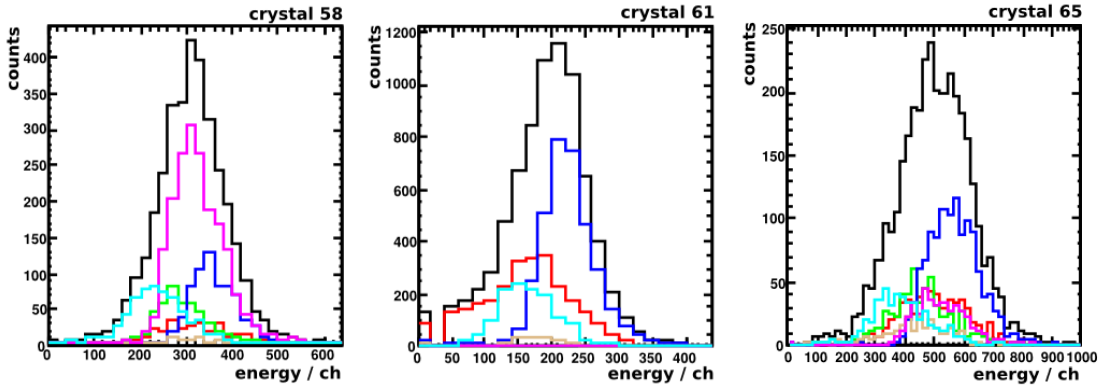

Figure 2.22: shows different energy deposits for different paths through crystals of shape B. The colors indicate what kind of path was travelled, i.e. red - from shape C to shape C crystal, green - B to D or D to B, blue B to C or C to B, light brown - B to B, pink - A to D or D to A, turquoise - A to C or C to A, and black is the sum of all. Crystal 58, shows standard crystal where the A-B-D transition governs, crystal 61 is a crystal where this transition as well as the B-B-D transitions are completely suppressed as the D neighbor is missing, and crystal 65 is a sample for a crystal where all transitions are present without a prominent one (though B-B-C is quite strong).

shape B crystals in different directions.[14] One can see frequently that one specific track governs the majority of crystals of a particular shape as indicated in Fig. 2.22, for a full comparison see A.1. Though, except for shape A (pentagonal), for all shapes a few crystals are not following the general pattern and the expected dominant track is not or only faintly observed. In these cases other tracks may be favored as sometimes it is the case for shape B crystals, or, as for shape C crystals, no track is dominant and the peak is a compound of several different tracks, each with about the same amount of counts. This is caused by the positioning of the crystals. The position can affect the muon distribution traversing a crystal in different ways. The modifications are partly due to detector electronics and partly due to its geometry. For example crystal positions which are empty (e.g. because a beampipe or targetholder is mounted there instead) cannot form a chain thereby suppressing a specific track for a neighboring crystal, but also enhancing other chains as the constraint that the neighbor ought not to have detected a signal is always true in case the respective neighbor is missing. Electronics also favors certain chains and thus tracks, as the trigger for muon events (the L+R muon trigger), see Fig. 2.2, requires both left and right half of the XB to have seen a signal above threshold, thus suppressing chains which only go through one half of the Crystal Ball. The other influence is the distribution of muons, i.e. their intensity is both energy and angle dependent, as well as angle and energy are correlated. Kempa found an empirical formula to describe the distribution, presented in [25, 26] and illustrated in Fig. 2.23. Due to the above illustrated position dependent energy deposit from the muons in single crystals of the Crystal Ball it is insufficient to simply calculate the pathlengths for each possible track for each crystal shape in order to infer the energy deposit from that. This is because of the fact that the distribution of paths is different for different crystals. Thus it is best to perform a simulation using a correct muon distribution and taking the Crystal Ball geometry into account.

The empirical formula from Ref. [26] and [25] for the absolute differential muon intensity is applicable for a momentum region between 0.2 GeV/c and $5 \cdot 10^4$ GeV/c and an angular range from vertical to horizontal. The momentum range fits our purpose as higher momenta have negligibly low intensities and lower momentum muons are stopped

[14] Note that it is only possible to compare the shifts for each crystal alone, since working with raw data and due to different gains on different crystals it is not possible to quantitatively compare the crystals at this point.

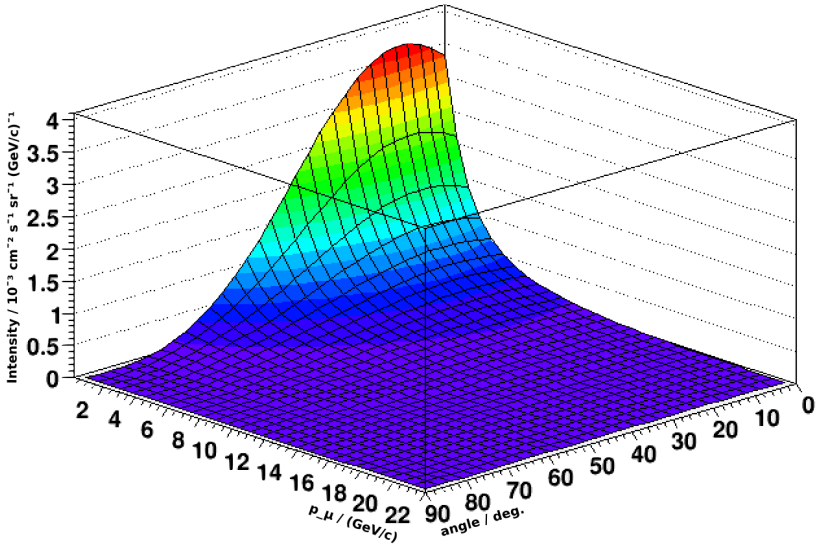

Figure 2.23: Plot illustrating the cosmic muon distribution at water level, showing the intensity depending on the absolute value of momentum and angle, formula from [26].

by the concrete surrounding the experimental setup. Comparing the result of the formula at 0° from the vertical direction at different momenta with the measurements presented in Ref. [27] one can see that the formula is representing the measured data well.
Thus, one can use this formula as input for a simulation, though not yet done. A possible framework is GEANT3 for which an implementation of the geometrical structure already exists. The general idea is to place the XB under a halfsphere of concrete which has an average thickness of the concrete walls of the cave, to ignore other obstacles like the ALADiN magnet, and to "shoot" muons according to the distribution onto it from outside the concrete sphere. If this turns out to be too much of an approximation one may be required to take the magnet and the support of the XB into account as well. Generating random muons impinging on the concrete sphere according to the distribution presented is nontrivial and a still ongoing work mainly done by H. Johansson.

3 The MPPC-Project

Multi-Pixel-Photon-Counters, short MPPCs, are an alternative read-out for scintillators. They belong to the category of Silicon-Photo-Multipliers, SiPMs, and can be thought of as an array of very tiny APDs, Avalanche-Photo-Diodes[28].
An APD is a photodiode operated in Geiger mode. Once a photon enters the diode and is absorbed, it creates an electron-hole pair. The charge carriers are due to the (comparably) strong electric field accelerated such that they create further electron-hole pairs by impact ionization as they collide with other charge carriers, creating an avalanche. In order to achieve this, the APDs are operated slightly above break-down voltage and the created avalanche is quenched by a resistor, resulting in a specific charge for each discharge which is caused by only one photon[1)] [29]. A MPPC is an array of several hundreds of APDs all operated in Geiger mode as described above. Each pixel, i.e. APD, can count zero or one photon (discharge or no discharge) and thus the MPPC as a whole has very good photon counting abilities and high photon detection efficiencies [30]. MPPCs are usually about 9 mm^2 or smaller, but are also produced in arrays [31]. They are highly competitive alternatives to the standard PM-tubes as scintillating detector or Cherenkov detector read-out [32], as they need lower operating voltage, are cheaper, and have high efficiency and fast timing [28]. They are also (as they are solid state devices) insensitive to magnetic fields and very compact. Their limited area might be a drawback when working with large volume scintillators, though it is, due to their high efficiency, probably possible to only cover a fraction of a scintillator backside.
Though MPPCs are a new product they are already planned to be employed in physics experiments like T2K. [33]

[1] During a discharge other photons could of course impinge on the cell which would not be detected.

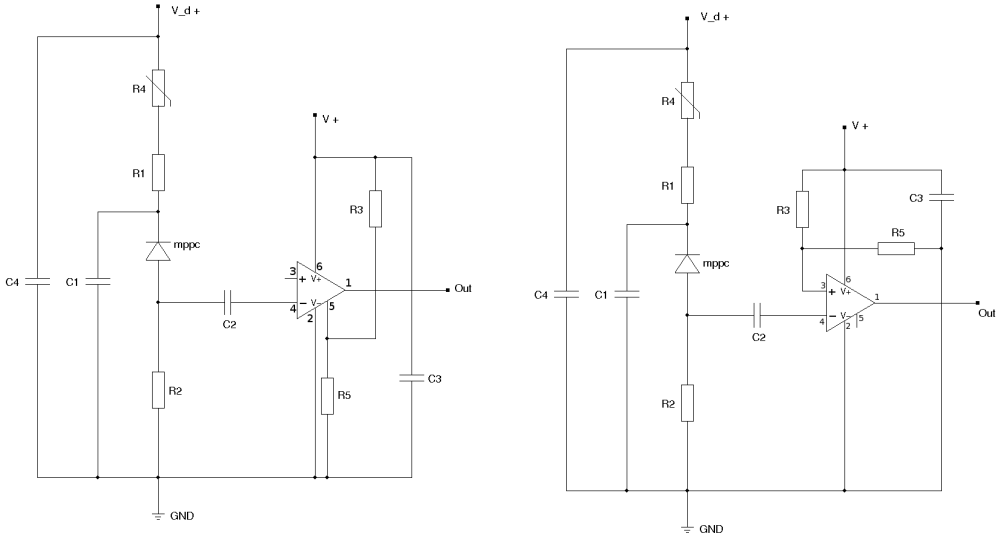

(a) received circuit

(b) realized circuit

Figure 3.1: The circuit drawings for setup number one. The left drawing (a) displays the circuit received and the right drawing (b) shows the circuit realized. Due to incompatibility of board and circuit drawing, modifications were necessary.

In this work first tests on a Hamamatsu S10931-025P MPPC were performed, in order to investigate if they are able to replace PM-tubes as read-out of the planned NeuLAND detector for the R^3B setup at GSI/FAIR. Employing them it may be possible to reduce production costs as they are cheaper.
Since MPPCs have a small signal amplitude it is necessary to amplify their signal at the first possible stage. Therefore they are mounted on circuit boards which supply the operating voltage but also amplify the output of the MPPCs directly, before sending it via cables to a more powerful amplifier further away. The arrangement of supply and amplifying circuit determine the performance of the device, and two different ones are presented in the following sections.

3.1 The different circuit board layouts

The detector laboratory at GSI developed two possible layouts for the circuit board processing MPPC signals. The first that was tried out was given as a circuit drawing, displayed in Fig. 3.1(a). As the board layout does not allow the assembly of that circuit because the standard operational amplifiers have their legs placed such that, making sure in-, output and power supply were correctly connected, it is not possible to have the legs 3 and 5 as displayed in Fig. 3.1(a). Therefore, it became necessary to modify the circuit as presented in Fig. 3.1(b).
The second circuit board layout is defined in a more peculiar way, by a mapping of the components on the board itself, as shown in Fig. 3.2(a). This layout translates together with the board (shown in Fig. 3.3) into a circuit as displayed in Fig. 3.2(b). The values of the capacitors and resistors are indicated in the figures, and the operational amplifier was chosen to match or exceed the specifications of the one used at GSI. In this work an OPA691 (Texas Instruments) with a bandwidth of 280 MHz and a slew rate of 2100 V/μs (see Ref. [34]) was used. This model is actually faster than the LT6230 (Linear Technology) employed at GSI. The two boards were assembled with the help of Björn Carlberg from the bionanosystems department, who provided also equipment for soldering of the individual components.

3.2 Assembly and setup of the circuit boards including the MPPC

The assembly of the boards was accomplished in several steps, first all components except the MPPC were soldered to the board (one side), then the MPPC was soldered to the other side, both in a temperature-controlling oven that followed a preprogrammed temperature profile. Afterwards cables for bias supply and read-out were soldered to the board by hand. A fully assembled board is shown Fig. 3.3. The board was connected to two power supplies (one providing power for the operational amplifier and one for the high voltage supply of the MPPC) and to the read-out which was realized either directly to an oscilloscope or via an additional fast amplifier.

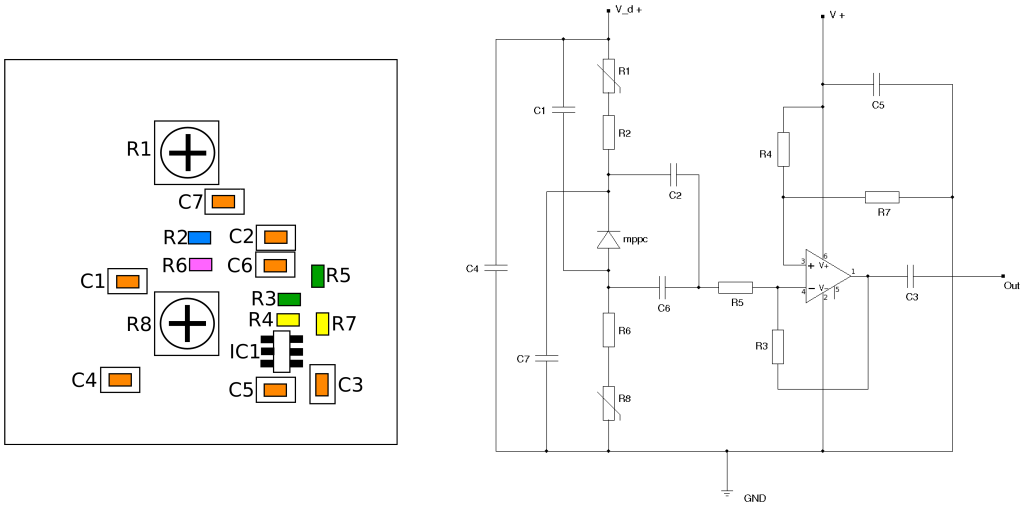

(a) Received image of components on board

(b) deduced circuit

Figure 3.2: (Circuit) Drawing illustrating the second setup realized. The left image (a) shows the image received which illustrates the distribution of components on the board. The right image (b) displays the from (a) and the circuit board deduced circuit.

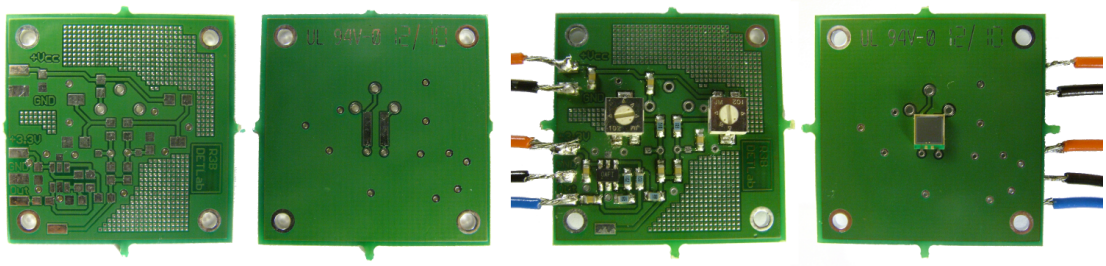

Figure 3.3: Photographs of an empty and an assembled board. The left two images show the empty board, and the two on the right an assembled board according to setup two. The left of each pair (empty/assembled) displays the side on which all components are mounted and the right image of each pair the side on which the MPPC is assembled (as can be seen in the rightmost picture).

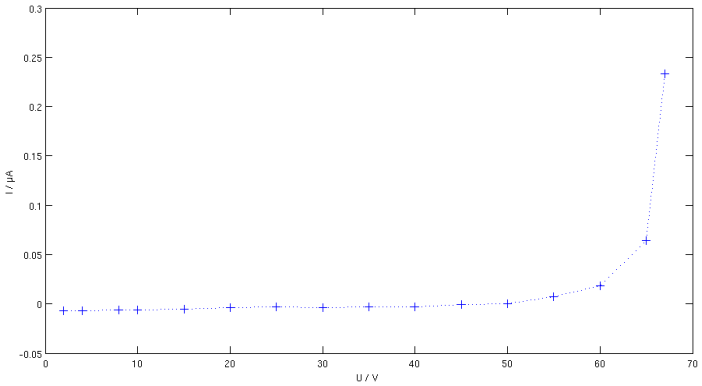

Figure 3.4: Graph showing the current over the MPPC depending on the (reverse) voltage applied. The measured points are marked with crosses and the dotted line is displayed to guide the eye. One can see the expected behavior.

3.3 Measurements with the MPPCs

After soldering the first board and confirming that all components were conducting, respectively insulating, the read-out of the first board was connected to the oscilloscope and the power to the amplifier was switched on. Noise could be observed, such that it was concluded that the amplifier is in working condition.
Next, the board (and thus the MPPC) was placed into a cardboard box wrapped in aluminum foil in order to shield it against electromagnetic noise and light. The box featured a pinhole to let light inside in a controlled way. With amplifier supplied with bias the voltage across the diode was ramped up slowly to the operating voltage of 72.6 V. No signal change was observed during that phase. When the small hole was opened, also no signal change could be observed.
As a consequence, the current through the MPPC was measured in order to ensure that the MPPC had not been damaged and behaves as expected for a diode. The result, presented in Fig. 3.4, confirmed this. Though no signals from individual photons could be identified on the oscilloscope, it showed the expected behavior of an MPPC, as, once

the pinhole was uncovered, the current increased. Still no signals could be seen when an additional fast amplifier was employed for additional filtering and amplification of the output signal of the board. Then the second setup was assembled and tried out as well. Again, all components were tested to be working correctly. Also for that setup no signals could be identified on the oscilloscope with and without an additional fast amplifier. In order to reduce the possibility of missing the signal in noise the two trim resistors were tuned in order to minimize the high frequency noise. This did not lead to any improvement in terms of signal observation.
In summary, with those two setups no proper signals were observed. This behavior might be due to several reasons. Most probable is that the operational amplifier is still too slow. The MPPC is supposed to provide a timing resolution of 600 ps [28] while the amplifier has a rise-/falltime of 1.6 ns and 1.9 ns respectively [34], which supports this hypothesis. Another reason might be the light, whose intensity through the pinhole might have overwhelmed the MPPC. However, no overall increase of the voltage of the output signal was observed when the current increased (due to light) close to the operating voltage. Thus, a problem with the circuit layout cannot be excluded at this point.
A new suggestion coming lately from GSI, which has already been tested successfully there, is to work without operational amplifier and to couple the signal directly to a standard QDC. Since this worked, there must have been a problem with the amplifier (or the circuit of the amplifier).

4 Discussion and summary

4.1 Discussion

Different calibration steps, for the Crystal Ball γ and proton detector of the LAND-setup have been studied, performed and analyzed.
Three different efficiency calibration methods of the XB were investigated, and one (the counting method) could be identified to be skewing the results. This method though is very stable and does not require very good statistics or special runs. It may therefore be desireable to find a way to correct this method. This could possibly be realized by classifying the crystals in different groups, according to the amount of material that is between target-position and crystal. The triggering would then only be allowed by crystals which are not subject to material in the path, thus not skewing the normalization counts. When working with such a discrete group of crystals though, one will have to take angular correlation effects into account for each crystal separately. Of course geometrical correction factors will also change. This therefore results in more calculational work but this way one might be able to recover the method. The other two methods are already working correctly, though the single crystal method needs longer data taking.
Considering these three methods in the context of the new detector CALIFA, which will replace the XB when transforming the LAND-setup to R^3B-setup, all of them face problems. CALIFA will be highly granular [35, 36], resulting in more channels / crystals to be calibrated. This has two consequences: the routines need to be stable such that no user interference is needed and the time to take data sets with enough statistics for

each crystal will increase (given same activity of the used sources). As only the barrel[1)] is estimated to have about 4000 crystals [37] this increase of crystals is of the order of a factor of 25 and larger (depending on the end caps). This has different results for the different methods; the sum-peak method used data collected during 21.5 h, each crystal now subtending only about 1/25 of the previous solid angle, resulting in more than 22 days data taking for CALIFA, not taking into account the stronger effect on the sum peak. The counting method does not need such long measurements, needing now about 15 min for a reasonable fitting, resulting in 5 to 6 days with CALIFA when all crystals can be used for triggering. As this will not be the case this will increase even further. These two methods are thus not practical for CALIFA. Considering to use the single crystal method with 10 s (which would probably be appropriate) for each crystal this amounts to (at least) 40000 s, a little more than 11 h, but not taking into account the smaller solid angle subtended! Assume that each crystal will subtend an angle of 1/25 of the XB crystals, corresponding to about 11.5 days for CALIFA. So also this method seems impractical. This situation changes with CALIFA being able to run triggerless, as such crystals do not interfere with each other concerning dead-time and therefore standard source data taken can be treated with the single crystal method. This leads to 10 seconds needed for each crystal times the solid angle factor amounting to 250 s, this is shorter than the time needed for the single crystal method of the XB (which needs triggers). One additional problem has not been taken into account yet in these calculations; the effect that smaller crystals are more affected by scattering leading to only partial absorption of the energy by each crystal. This probably requires[2)] an addback algorithm to be applied before doing an efficiency calibration. If this is so the single crystal method faces a problem, as deadtime of the clusters would have to be determined.

Pending the necessity of addback before efficiency calibration, the best method for the efficiency calibration of CALIFA, is still not sure. If addback is not necessary the single crystal method is clearly the best choice, if it is necessary the corrected counting method might be more applicable.

If addback is indeed necessary in order to get full energy peaks in the spectra, even for the time and energy method (which definitely need to be done before addback) new

[1] The design of CALIFA is divided into a barrel part surrounding the target and two end caps closing the backward and the forward direction (except for the beamline of course), see Ref. [36] for details.

[2] This needs to be simulated to be sure on the magnitude of this effect.

calibration methods need to be found.
The muon calibration seems to be transferable to CALIFA, one needs to find new well-defined paths of course, but once the simulation is set up one can replace the detector and check what kind of paths are useful for energy calibration of the proton read-out. The big advantage using muons is that cosmic data is collected always during offspill, and can easily be collected in beam interruptions, etc. such one does not necessarily need extra time collecting data for calibration.

4.2 Summary

In the course of this work calibrations of the γ and proton detector XB from the LAND-setup at GSI, were analyzed.
Time and γ-branch energy calibration were performed for the Crystal Ball. A preliminary proton-branch calibration was done as well, and a method how to complete this calibration was proposed. The completion needs a simulation of cosmic muons traversing the Crystal Ball, and a suggestion how to realize this was presented. Concerning the efficiency of the detector, three methods were studied. For all three methods, scripts were written to do the calibration automatically. One of these, the counting method, disqualified because it skews the results. Another one, the single crystal method, was found not trustable due to low statistics. The sum-peak method was asserted to be appropriate for calibration of the S393 (and s389) experiment(s). Taking an outlook to CALIFA, the replacement detector of the XB, one needs to conclude that the sum-peak method, because it needs very good statistics, will not be feasible. Therefore the single crystal method is suggested to be used in further experiments with an extended measurement time which will still be much shorter than the time needed for the sum-peak method.
The second project of this work was to test an alternative read-out system for the planned neutron detector of the R^3B setup, NeuLAND. The MPPC's are supposed to be highly photosensitive but much cheaper than conventional PMT's. Two ways of amplifying the signal of the MPPC's, by an operational amplifier sitting on the circuit board on which the MPPC is mounted, were tested. None of these worked though the single components function was verified. As tests without operational amplifier, worked out well at GSI it

is concluded that the available operational amplifier was too slow.

Glossary

APD Avalanche Photo-Diode, a photo diode operated in Geiger mode in order to detect incoming photos for low luminosities

ADC Analog to Digital Converter, converts the maximum amplitude of an analog signal (in a fixed time interval) into a digital signal

BLR BaseLine Restorer, a component in signal processing forcing the signal back to zero level in order to prevent pile-up

CALIFA CALorimeter for In-Flight emitted gAmmas and light charged particles for R^3B, planned new proton and γ detector to replace the XB in the course of the transformation of the LAND-setup to the R^3B setup

CFD Constant Fraction Discriminator, electronic device to determine the timing of a pulse independent of the height

FAIR Facility for Antiproton and Ion Research, GSI will be enlarged and internationalized to become this facility

GSI Gesellschaft für Schwerionenforschung in English: society for heavy ion research, a national research facility located at Darmstadt to be transformed into international FAIR

LAND Large Area Neutron Detector, as the name tells a neutron detector out of iron degrader material and plastic scintillator read out by PM-tubes, so important that

the whole experimental setup it belongs to is referred to as the LAND-setup

LED Leading Edge Discriminator, device to determine the timing of a pulse, with dependence on the pulse-height

MPPC Multi-Pixel-Photon-Counter, a name used by Hamamatsu for one of their Si-PM, basically an array of APDs

MSCF Mesytec Spectroscopy amplifier with Constant Fractions, a module used for the XB splitting and amplifying the analog signals, preparing it for TDC, ADC and producing trigger signals

PM-tube PhotoMultiplier-tube, usually used to transform scintillation light into electronic pulses

NeuLAND new neutron detector to be built for R^3B replacing the LAND detector, it will consist completely of plastic scintillator paddles

R^3B Reactions with Relativistic Radioactive Beams, name of the LAND setup will be transformed to

Si-PM Silicon PhotoMultiplier, solid state device based on Silicon which collects light and transforms it into an electronic amplified pulse, similar application area as the PM-tube

SSD Silicon Strip Detector, a detector made of this silicon strips for position and ΔE measurement, located around the target in the LAND-setup

TDC Time to Digital Converter, transforms a timing pulse into a logical timing signal

XB Crystal Ball, the proton and γ-detector of the LAND setup

Bibliography

[1] IUPAC in conjunction with IUPAP: *Discovery of a new chemical element to be recognized*. Pure and Applied Chemistry, 1991.

[2] J. Magill, G. Pfennig, and J. Glay: *Karlsruher Nuklidkarte*, 2007.

[3] Maria G. Mayer: *On closed shells in nuclei.* Phys. Rev., 74(3):235–239, Aug 1948.

[4] Maria G. Mayer: *On closed shells in nuclei. II.* Phys. Rev., 75(12):1969–1970, Jun 1949.

[5] Maria G. Mayer: *Nuclear configurations in the spin-orbit coupling model. I. empirical evidence.* Phys. Rev., 78(1):16–21, Apr 1950.

[6] Björn Jonson: *Light dripline nuclei.* Physics Reports, 389:1 – 59, January 2004.

[7] The R^3B Collaboration: *Neutron-rich nuclei at and beyond the dripline in the range z=4 to z=10 studied in kinematically complete measurements of direct reactions at relativistic energies*, Experiment Proposal, 2009.

[8] W.R. Leo: *Techniques for Nuclear and Particle Physics Experiments A How-to Approach*, chapter 7. Springer-Verlag, 1994.

[9] Ralf Plag: *land02 - featuring the unofficial guide to the unofficial version of land02.* http://www-linux.gsi.de/~rplag/land02/.

[10] V. Metag, R.D. Fischer, W. Kühn, R. Mühlhans, R. Novotny, D. Habs, U.v. Helmholt, H.W. Heyng, R. Kroth, D. Pelte, D. Schwalm, W. Hennerici, H.J. Hennrich, G. Himmerle, E. Jaeschke, R. Repnow, W. Wahl, E. Adelberger, A. Lazzarini, R.S. Simon, R. Albrecht, and B. Kolb: *Physics with 4-π-γ-detectors.* Nucl.Phys., A409:331c –342c, 1983.

[11] D. Habs, F.S. Stephens, and R. M. Diamond: *A proposal for a Crystal-Ball detector system.* Technical report, Lawrence Berkeley Laboratory, 1979.

[12] Dipl. Phys. Felix Wamers: *Quasi-free Knockout Reactions with the Proton-dripline Nucleus ^{17}Ne.* PhD thesis, TU Darmstadt, 2011.

[13] H.T. Johansson and Yu. Aksyuntina: *An algorithm for offline correction of the walk effect.* Technical report, GSI, 2009.

[14] Felix Wamers: *Readme.* readme file coming with the calibration script package for the XB gamma branch.

[15] Håkan Johansson: *gamma2 time synchronisation.* personal communication, April 2011.

[16] Rene Brun: *ROOT - a data analysis framework.* Website: http://root.cern.ch/drupal/.

[17] Mesytec: *Manual - MSCF 16 F.* www.mesytec.com/datasheets/MSCF-16-F.pdf.

[18] Nigel Warr: *Miscellaneous programs for Miniball.* www.ikp.uni-koeln.de/~warr/doc/misc_progs.pdf, 2010.

[19] Z. Hu, R. Collatz, H. Grawe, and E. Roeckl: *Energy and efficiency calibration of an array of six Euroball Cluster detectors used for beta-decay studies.* Nucl.Instrum.Meth., A419(1):121 – 131, 1998.

[20] T. Vidmar, M. Korun, and A. Likar: *Close-geometry efficiency calibration in gamma-ray spectrometry using radio-nuclides with a two-step cascade decay.*

Nucl.Instrum.Meth., A508(3):404 – 413, 2003.

[21] Kai Siegbahn (editor): *Alpha-, beta- and gamma-ray spectroscopy.* American Elsevier Publishing Company, 1965.

[22] Donald R. Hamilton: *On directional correlation of successive quanta.* Physical Review, 58, 1940.

[23] Richard B. Firestone: *Table of Isotopes.* John Wiley and sons, 8th edition, 1996.

[24] *Nuclear Data Tables A7*, chapter p. 565. 1970.

[25] J. Kempa and A. Krawczynska: *Low energy muons in the cosmic radiation.* Nucl.Phys.Proc.Suppl., 151:299–302, 2006.

[26] J. Kempa and I.M. Brancus: *Zenith angle distributions of cosmic ray muons.* Nucl.Phys.Proc.Suppl., 122:279–281, 2003.

[27] Sadakazu Haino, T. Sanuki, K. Abe, K. Anraku, Y. Asaoka, *et al.*: *Measurements of primary and atmospheric cosmic - ray spectra with the BESS-TeV spectrometer.* Phys.Lett., B594:35–46, 2004.

[28] HAMAMATSU: *Technical data sheet for MPPC S10931 series.* www.hamamatsu.com.

[29] Junji Haba: *Status and perspectives of Pixelated Photon Detector (PPD).* Nucl.Instrum.Meth., A595:154–160, 2008.

[30] S. Gomi, H. Hano, T. Iijima, S. Itoh, K. Kawagoe, S.H. Kim, T. Kubota, T. Maeda, T. Matsumura, Y. Mazuka, K. Miyabayashi, H. Miyata, T. Murakami, T. Nakadaira, T. Nakaya, H. Otono, E. Sano, T. Shinkawa, Y. Sudo, T. Takeshita, M. Taguchi, T. Tsubokawa, S. Uozumi, M. Yamaoka, H. Yamazaki, M. Yokoyama, K. Yoshimura, and T. Yoshioka: *Development and study of the multi pixel photon counter.* Nucl.Instrum.Meth., A581(1-2):427 – 432, 2007.

[31] HAMAMATSU: *Website*. www.hamamatsu.com.

[32] P. Buzhan, B. Dolgoshein, L. Filatov, A. Ilyin, V. Kantzerov, V. Kaplin, A. Karakash, F. Kayumov, S. Klemin, E. Popova, and S. Smirnov: *Silicon photomultiplier and its possible applications*. Nucl.Instrum.Meth., A504(1-3):48 – 52, 2003.

[33] Antonin Vacheret: *Characterization of the 1.3 mm · 1.3 mm mppc for the T2K near detectors*. Nucl.Instrum.Meth., A623(1):201 – 203, 2010.

[34] Texas Instruments: *OPA691 wideband, current feedback operational amplifier with disable*. www.ti.com, July 2008.

[35] The R^{3}B Collaboration: *R^3B - A universal setup for kinematical complete measurements of reactions with relativistic radioactive nuclei*. Technical report, http://www.gsi.de/forschung/kp/kr/R3B/Documents_e.html, 2005.

[36] H.A. Pol: *R^3B gamma calorimeter development*. Website: http://www.usc.es/genp/.

[37] D.D. Dijulio, V. Avdeichikov, J. Cederkall, P. Golubev, B. Jakobsson, H. Johansson, and C. Tintori: *Proton in-beam tests of the Lund R^3B calorimeter prototype*. Nucl.Instrum.Meth., A612:127 – 132, 2009.

A Appendix

A.1 Muon simulation

In the following graphs A.1 - A.6 for all crystals are given, illustrating the effect of different lengths of chains for grazing muons. For all of the following plots applies that the different lengths of the chains are marked such that: black = 5, red = 6, green = 7 and blue = 8 crystals.
The subsequent graphs A.7 - A.12 illustrate different energy deposits by different paths through a crystal, for all crystals, with a cut on the chainlength to be 6 or 7 crystals. Also to be notes is that not all crystal feature all possible paths.

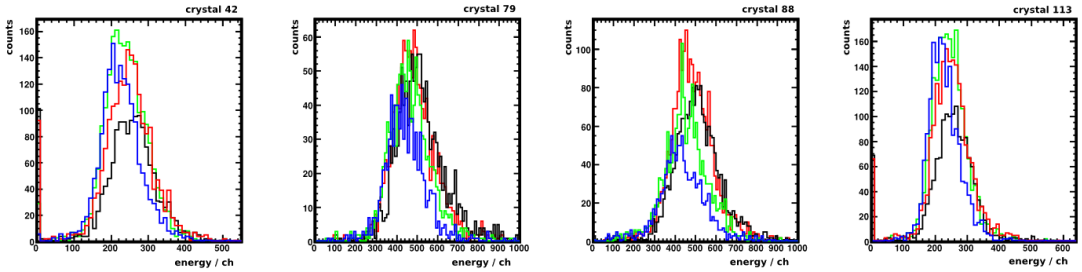

Figure A.1: Crystals of shape A, distribution of chains with different length.

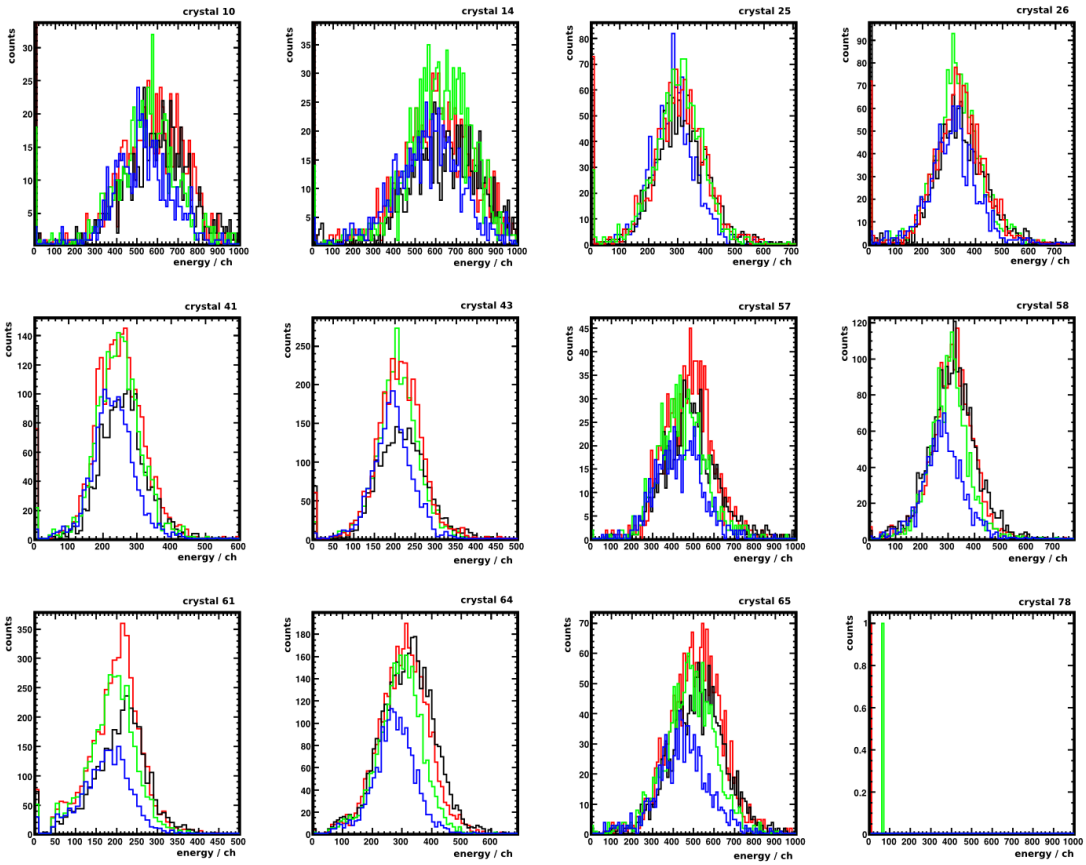

Figure A.2: Crystals of shape B, distribution of chains with different length.

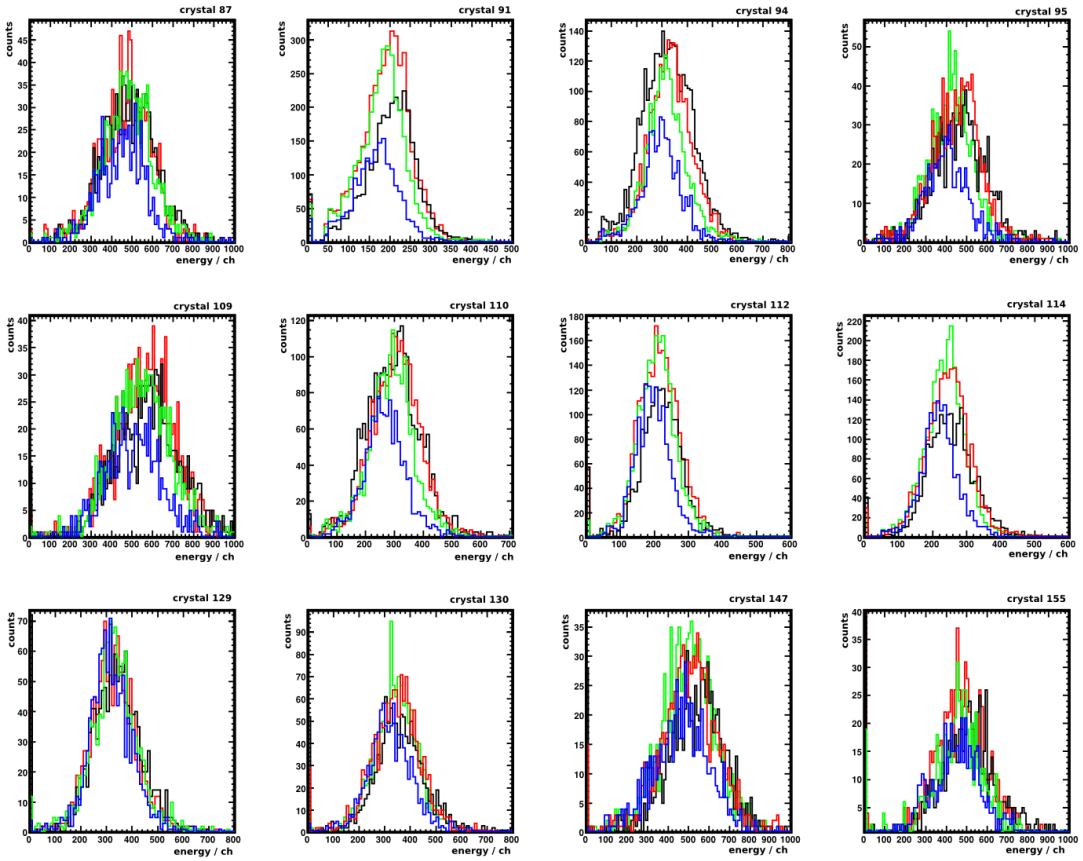

Figure A.3: Crystals of shape B, distribution of chains with different length.

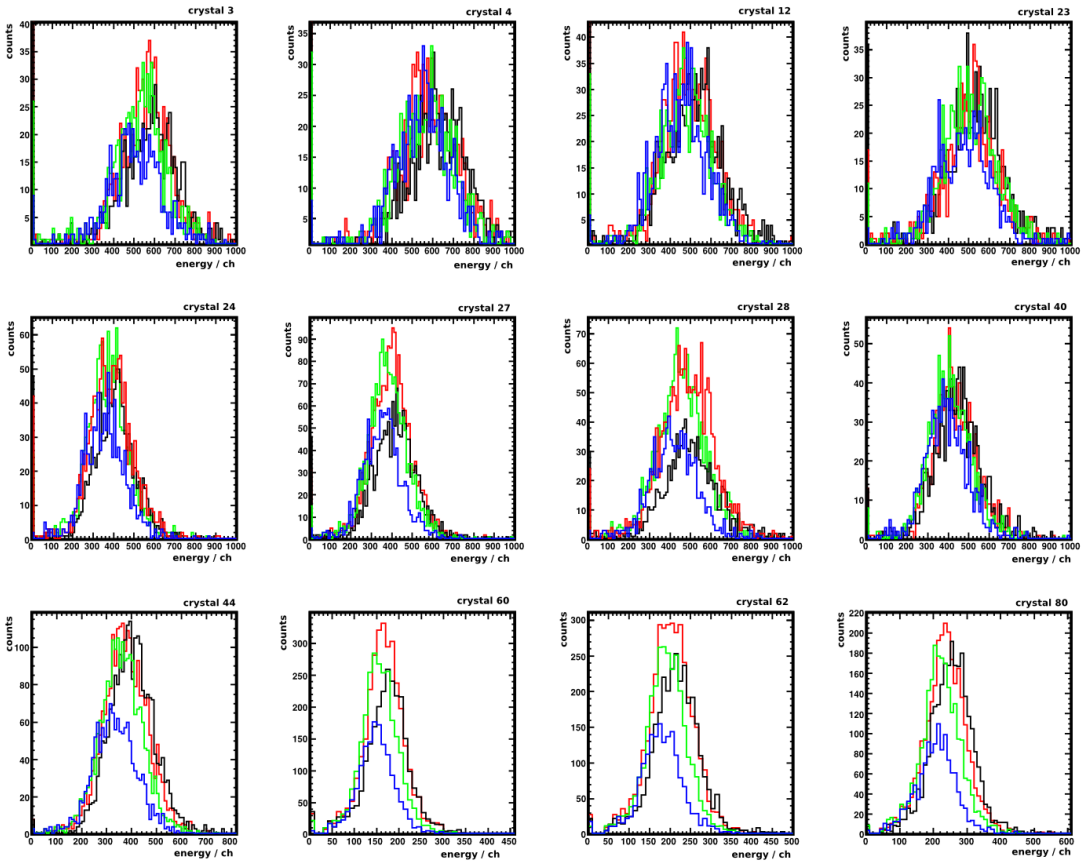

Figure A.4: Crystals of shape C, distribution of chains with different length.

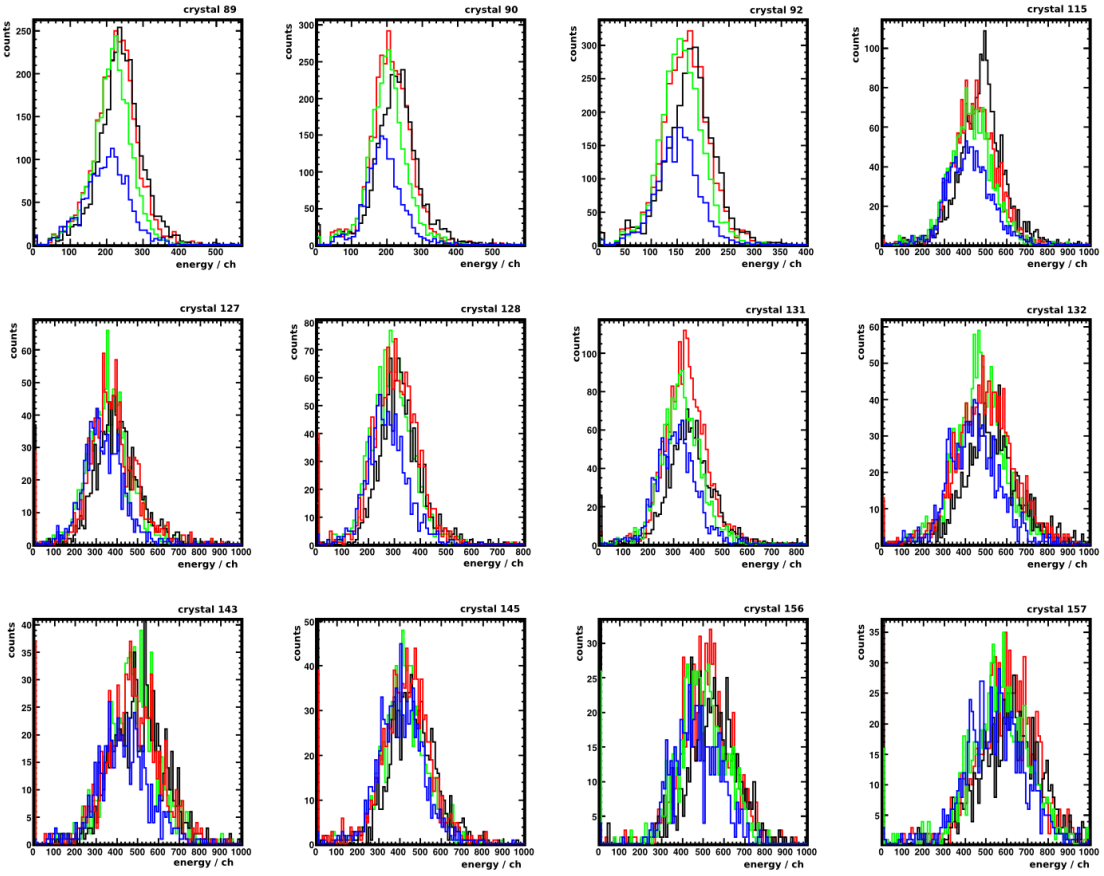

Figure A.5: Crystals of shape C, distribution of chains with different length.

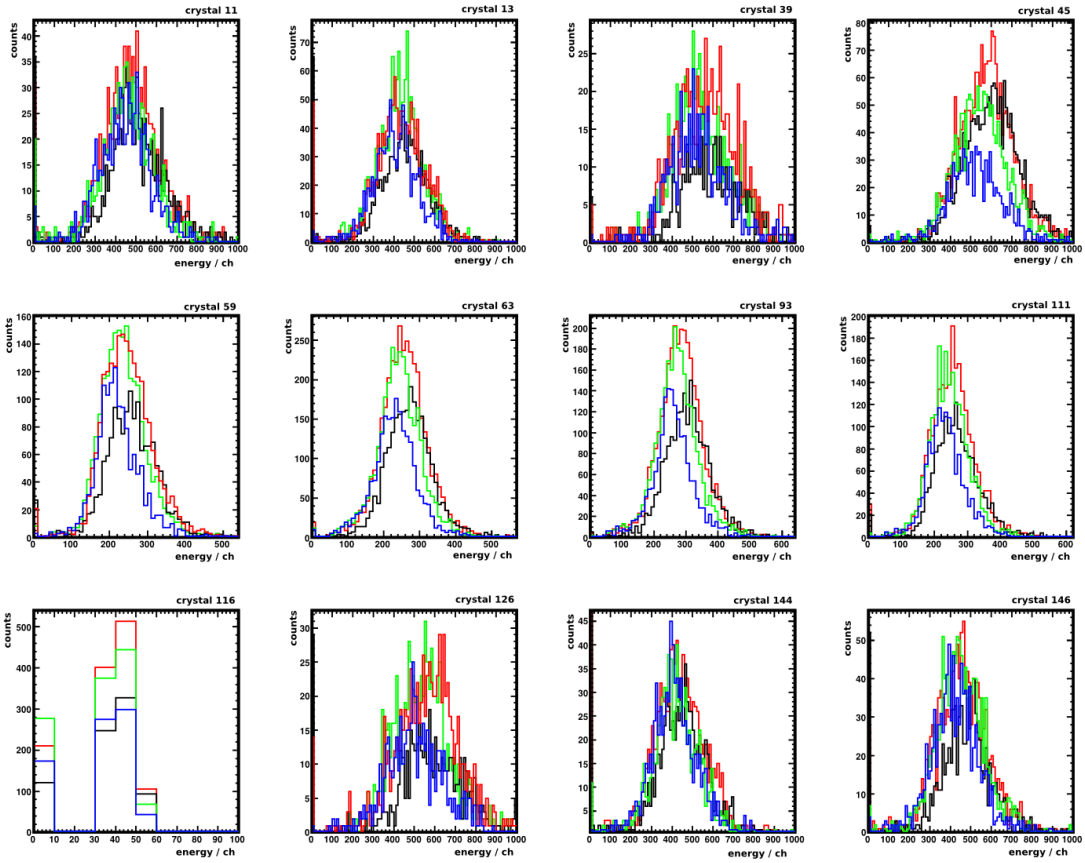

Figure A.6: Crystals of shape D, distribution of chains with different length.

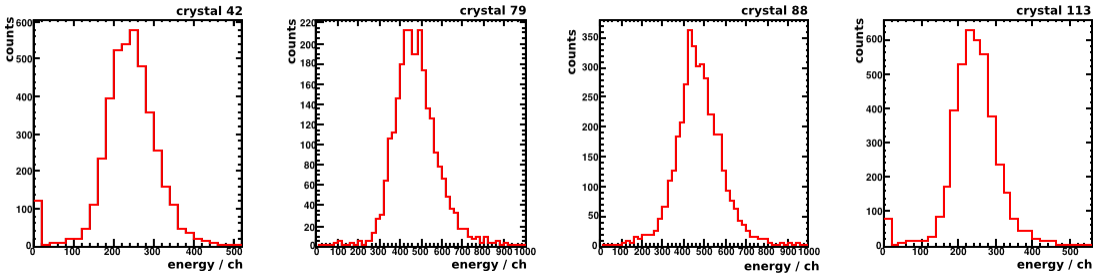

Figure A.7: Crystals of shape A, only one type of crossing a crystal of shape A is possible, as also seen in the picture.

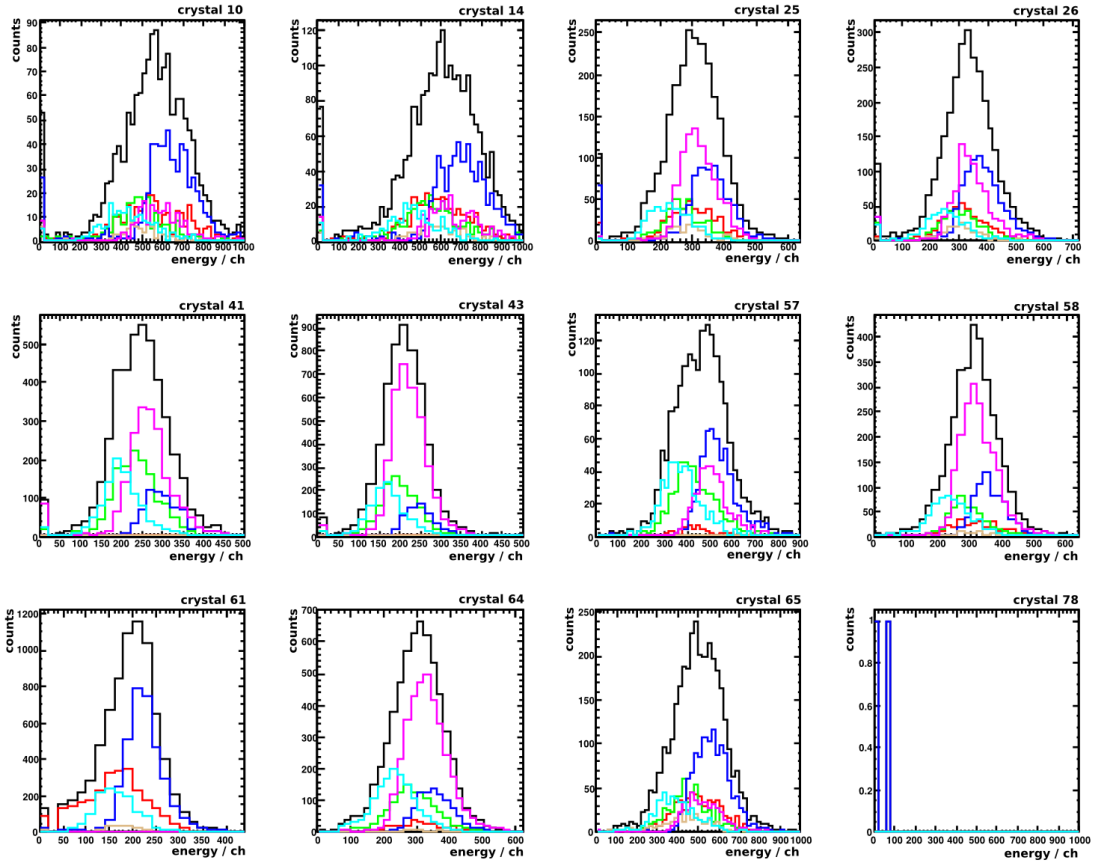

Figure A.8: Crystals of shape B for found chains of 6 or 7 crystals, colors indicating the different ways of crossing the crystal: black - sum on all, red - from shape C to shape C crystal, green - B to D or D to B, blue B to C or C to B, light brown - B to B, pink - A to D or D to A and turquoise - A to C or C to A. One can see that a large part of B crystals are mainly crossed by muons from A to D (or vice versa), but for the majority a composition of different crossings is giving rise to the energy deposit.

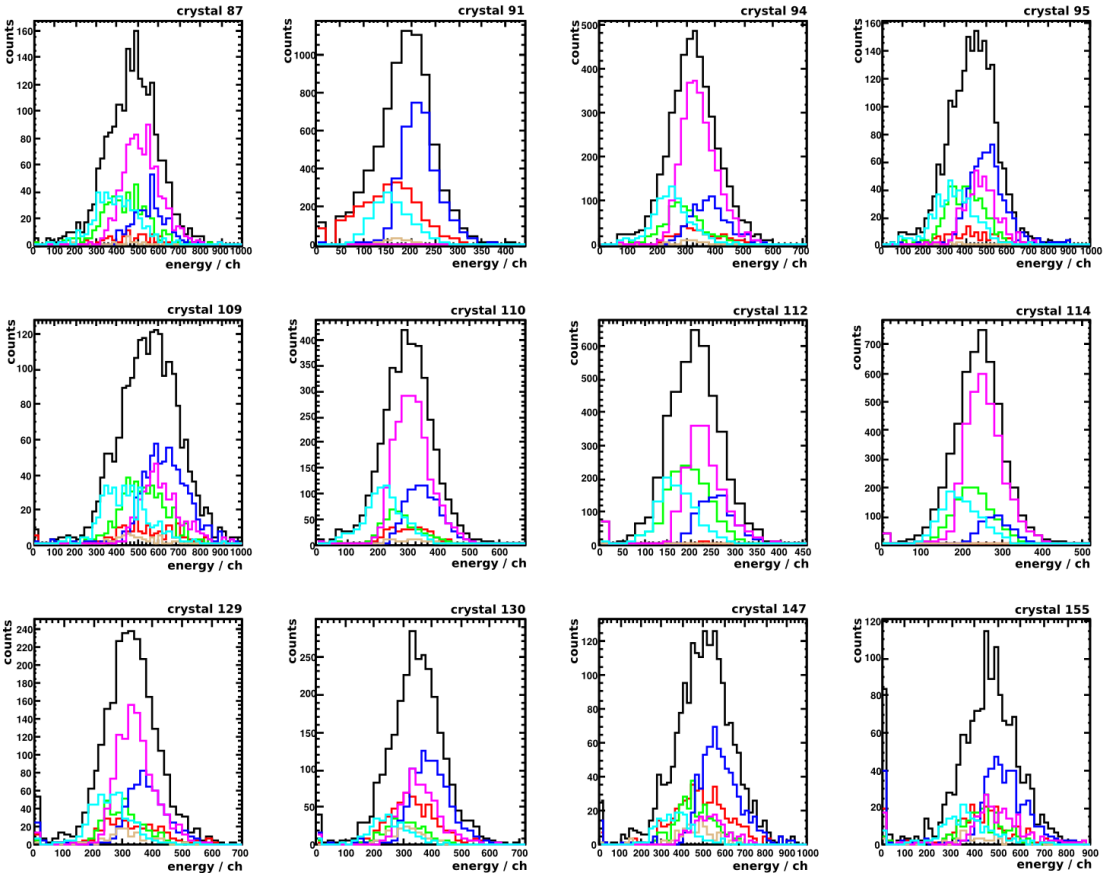

Figure A.9: Crystals of shape B for found chains of 6 or 7 crystals, colors indicating the different ways of crossing the crystal: black - sum on all, red - from shape C to shape C crystal, green - B to D or D to B, blue B to C or C to B, light brown - B to B, pink - A to D or D to A and turquoise - A to C or C to A. One can see that a large part of B crystals are mainly crossed by muons from A to D (or vice versa), but for the majority a composition of different crossings is giving rise to the energy deposit.

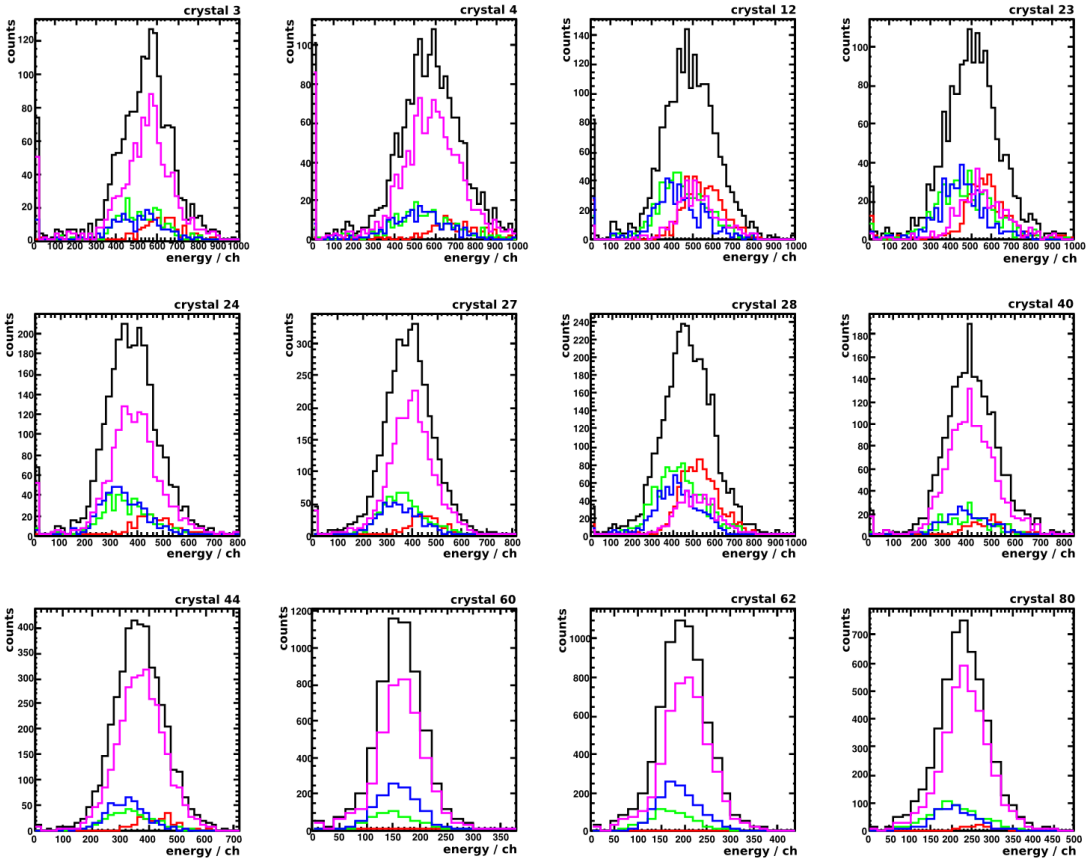

Figure A.10: Crystals of shape C for found chains of 6 or 7 crystals, colors indicating the different ways of crossing the crystal: black - sum on all, red - from shape D to shape D crystal, green - C to D or D to C, blue B to D or D to B and pink - B to C or C to B. The vast majority of crystals gets the largest part of energy deposit from a muon crossing from B to C (or vice versa). Note that this has a large variation in energy deposit due to the fact that the differentiation between a B-C-C transition where the outermost crystals are exactly across each other and a B-C-C transition where they are not had not been made at that point.

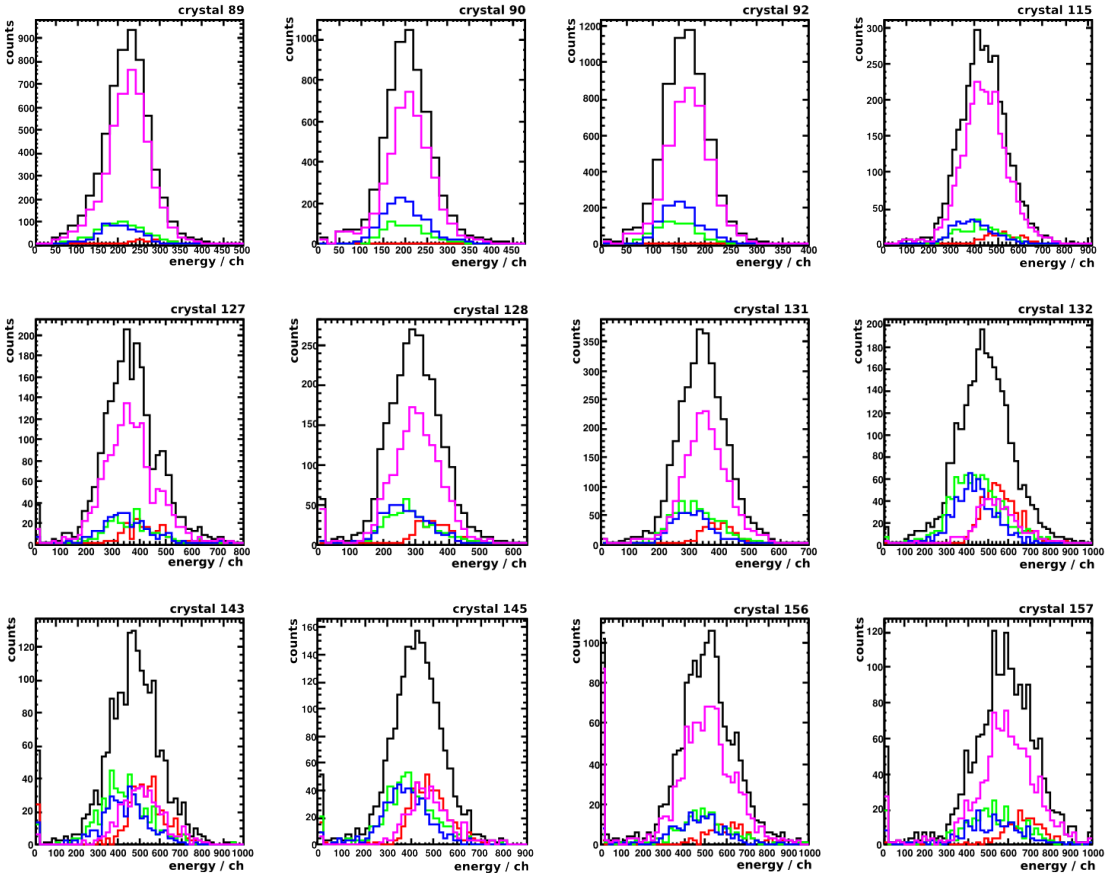

Figure A.11: Crystals of shape C for found chains of 6 or 7 crystals, colors indicating the different ways of crossing the crystal: black - sum on all, red - from shape D to shape D crystal, green - C to D or D to C, blue B to D or D to B and pink - B to C or C to B. The vast majority of crystals gets the largest part of energy deposit from a muon crossing from B to C (or vice versa). Note that this has a large variation in energy deposit due to the fact that the differentiation between a B-C-C transition where the outermost crystals are exactly across each other and a B-C-C transition where they are not had not been made at that point.

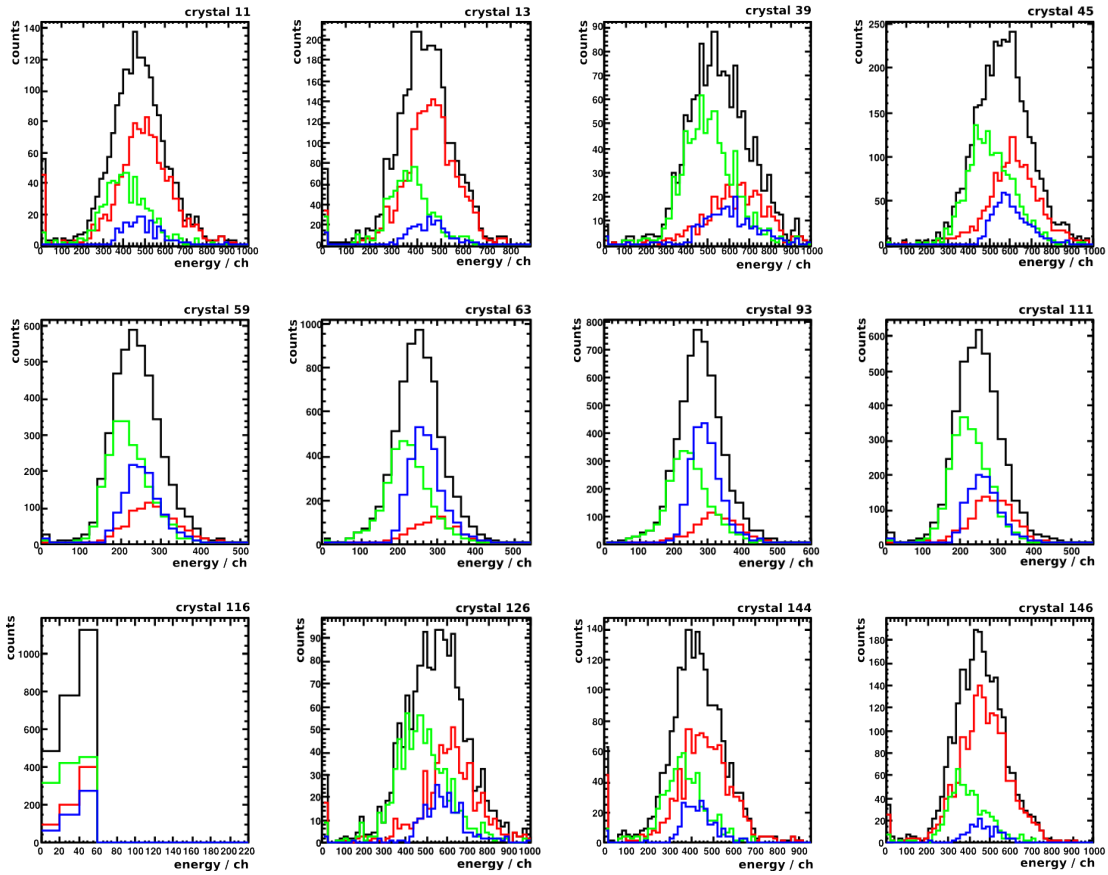

Figure A.12: Crystals of shape D for found chains of 6 or 7 crystals, colors indicating the different ways of crossing the crystal: black - sum on all, red - from shape C to shape C crystal and green - B to C or C to B, blue B to B or B to B. For these crystals there seems to be no general trend which crossing is important. Also here in the C-D-C transition there is an ambiguity as the differentiation between exactly across each other and not exactly across each other lying crystals had not been made.

A.2 Fitresults from the fit of the ^{60}Co-spectrum

This section will present a table of the fitresults from the fits of the ^{60}Co-spectrum which were used for the efficiency calibration.

detector	pos. $\gamma 1$	dpos $\gamma 1$	pos. $\gamma 2$	dpos $\gamma 2$	σ $\gamma 1$	dσ $\gamma 1$	σ $\gamma 2$	dσ $\gamma 2$
1	1181.27	0.12	1341.54	0.12	32.6	0.11	32.62	0.1
2	1179.64	0.12	1338.19	0.12	32.95	0.12	32.22	0.1
3	1178.57	0.13	1337.13	0.13	36.18	0.12	36.96	0.12
4	1189.69	0.14	1350.59	0.15	36.74	0.14	37.68	0.14
5	1180.72	0.15	1341.17	0.14	34.04	0.14	34.77	0.13
6	1183.34	0.13	1342.95	0.14	37.85	0.13	40.93	0.15
7	1182.69	0.7	1341.5	0.86	63.92	0.5	54.36	0.77
8	1190.98	0.22	1353.7	0.2	35.14	0.21	33.71	0.19
9	1174.67	0.21	1332.34	0.22	42.9	0.22	40.48	0.21
10	1179.07	0.11	1339.57	0.12	33.98	0.11	34.78	0.1
11	1178.48	0.19	1335.2	0.21	44.15	0.18	44.64	0.2
12	1178.55	0.24	1335.82	0.27	48.04	0.23	47.21	0.27
13	1190.11	0.13	1351.67	0.14	36.87	0.13	36.97	0.13
14	1180.75	0.17	1342	0.17	39.89	0.18	37.7	0.16
15	1175.52	0.14	1333.88	0.14	34.85	0.14	33.94	0.12
16	1171.83	0.12	1330.6	0.13	37.39	0.12	39.32	0.13
17	1176.02	0.09	1334.7	0.1	31.95	0.09	33.15	0.08
18	1177.09	0.12	1336.11	0.13	37.32	0.12	39.05	0.12
19	1181.89	0.22	1341.77	0.24	39.2	0.22	41.87	0.25
20	1192.49	1.11	1352.13	1.27	64.42	0.84	51.3	1.32
21	1166.12	0.54	1318.98	0.9	43.34	0.52	72.43	1.47
22	1190.66	0.17	1353.85	0.17	38.73	0.17	38.14	0.16
23	1171.86	0.13	1329.56	0.13	37.07	0.12	37.84	0.12
24	1177.82	0.18	1334.18	0.2	43.11	0.17	46.08	0.2
25	1180.54	0.11	1341.33	0.11	36.4	0.11	37.05	0.11
26	1183.27	0.17	1343.3	0.19	40.55	0.16	45.27	0.2
27	1180.22	0.16	1339.44	0.18	42.44	0.16	44.28	0.19
28	1180.82	0.21	1335.44	0.26	45.47	0.19	47.84	0.25
29	1176.03	0.19	1334.76	0.2	41.04	0.19	41.65	0.19
30	1178.8	0.12	1339.58	0.13	37.26	0.13	36.77	0.12
31	1180.91	0.1	1340.29	0.1	34.35	0.1	34.47	0.09

32	1176.83	0.1	1335.77	0.1	33.88	0.09	35.05	0.09
33	1178.37	0.13	1337.23	0.14	38.83	0.13	39.96	0.13
34	1174.89	0.12	1333.51	0.12	35.04	0.11	34.83	0.1
35	1178.05	0.32	1336.69	0.35	42.7	0.32	45.84	0.38
36	1179.22	0.2	1337.87	0.2	44.07	0.21	39.88	0.19
37	1175.85	0.13	1335.47	0.13	36.01	0.13	35.2	0.12
38	1186.61	0.2	1347.22	0.2	41.01	0.2	38.07	0.19
39	1182.94	0.16	1343.52	0.16	38.23	0.16	37.87	0.15
40	1185.87	0.14	1346.12	0.15	38.67	0.14	39.37	0.15
41	1172.06	0.21	1328.97	0.25	44.83	0.19	50.74	0.26
42	1189.86	0.12	1351.96	0.13	38.24	0.12	39.91	0.13
43	1192	0.19	1351.65	0.22	43.17	0.18	46.42	0.25
44	1184.12	0.16	1340.92	0.17	40.09	0.15	44.59	0.18
45	1178.22	0.16	1341.82	0.16	46.38	0.19	40.51	0.16
46	1176.59	0.22	1333.65	0.24	45.04	0.21	44.93	0.22
47	1172.81	0.15	1330.11	0.17	40.28	0.15	43.15	0.16
48	1179.03	0.1	1339.33	0.1	33.5	0.09	34.97	0.09
49	1204.12	0.97	1362.46	1.01	75.98	0.65	43.04	0.8
50	1177.09	0.12	1336.04	0.12	37.48	0.12	37.43	0.11
51	1175.3	0.13	1334.88	0.13	36.97	0.12	36.06	0.11
52	1186.12	0.99	1346.36	1.35	68.66	0.57	59.38	1.33
53	1173.26	0.22	1331.68	0.24	48.57	0.23	42.74	0.22
54	1178.88	0.23	1338.42	0.24	45.04	0.24	40.01	0.22
55	1180.45	0.24	1340.73	0.29	47.04	0.23	50.33	0.32
56	1185.93	1.24	1345.3	1.46	63.5	0.92	58.95	1.41
57	1186.94	0.17	1348.63	0.18	40.46	0.17	41.38	0.19
58	1186.61	0.18	1347.77	0.18	37.59	0.17	38.01	0.17
59	1185.65	0.15	1346.92	0.15	38.65	0.14	40.26	0.15
60	1192.77	0.17	1354.06	0.19	43.14	0.17	44.28	0.21
61	1174.68	0.18	1332.79	0.2	43.81	0.18	44.76	0.2
62	1177.03	0.16	1335.43	0.17	40.82	0.16	42.12	0.16
63	1178.28	0.24	1336.78	0.27	38.85	0.21	66.4	0.37
64	1179.43	0.16	1337.7	0.18	40.85	0.15	44.85	0.18
65	1187.77	0.19	1344.21	0.22	44.3	0.18	47.31	0.23
66	1176.94	0.24	1335.73	0.27	44.19	0.22	52.06	0.31
67	1181.72	0.12	1341.51	0.13	39.03	0.12	38.52	0.12
68	1176.37	0.14	1335.13	0.14	38.76	0.13	40.18	0.14
69	1171.61	0.1	1329.76	0.1	32.93	0.1	32.65	0.09

70	1171.29	1.06	1332.5	1.07	46.59	0.86	40	2.58
71	1182.55	0.61	1342.71	0.74	66.91	0.47	54.71	0.62
72	1172.72	0.1	1331.33	0.11	35.58	0.1	36.38	0.1
73	1181.44	0.26	1342.19	0.3	57.09	0.26	44.72	0.26
74	1176.44	0.12	1335.16	0.13	39.67	0.12	38.92	0.12
75	1175.35	0.2	1334.13	0.22	44.28	0.2	42.97	0.21
76	1176.94	0.21	1336.05	0.25	46.93	0.21	45.6	0.24
77	nan	nan	nan	nan	nan	nan	nan	nan
78	1171.29	0.03	1332.5	0.03	716.2	0.01	40	0.01
79	1186.86	0.32	1341.61	0.35	47.3	0.27	51.8	0.4
80	1187.01	0.14	1345.22	0.16	39.59	0.14	43.09	0.16
81	nan	nan	nan	nan	nan	nan	nan	nan
82	nan	nan	nan	nan	nan	nan	nan	nan
83	1177.26	0.15	1335.93	0.16	44.85	0.16	40.45	0.15
84	1179.83	0.13	1338.59	0.13	38.3	0.12	37.25	0.11
85	1176.47	0.12	1335.25	0.13	37.04	0.12	40.54	0.13
86	1174.79	0.19	1336.66	0.2	47.62	0.22	42.15	0.18
87	1183.08	0.14	1341.71	0.15	39.59	0.14	39.66	0.14
88	1193.13	0.13	1352.83	0.14	40.13	0.13	40.75	0.14
89	1176.29	0.24	1339.68	0.29	38.49	0.22	56.72	0.39
90	1186.27	0.16	1346.69	0.18	40.63	0.15	45.48	0.2
91	1181.83	0.22	1339.4	0.24	39.75	0.2	57.03	0.31
92	1183.31	0.34	1340.24	0.37	44.65	0.27	62.08	0.5
93	1186.69	0.17	1346.96	0.18	42.25	0.16	43.69	0.19
94	1171.23	0.19	1353.29	0.19	127.41	0.18	40	0.2
95	1185.57	0.15	1344.73	0.16	40.72	0.15	40.19	0.15
96	1174.29	0.2	1333.16	0.22	43.99	0.2	43.36	0.21
97	1175.08	0.12	1333.97	0.12	37.09	0.13	34.56	0.11
98	1176.02	0.18	1334.26	0.18	39.44	0.18	37.38	0.16
99	1178.3	0.14	1336.54	0.15	39.11	0.14	39.18	0.14
100	1171.23	0.41	1328.59	0.75	40	0.7	40	0.52
101	1168.98	0.59	1320.6	0.73	46.95	0.38	83.26	0.93
102	1169.79	0.1	1328.16	0.11	35.7	0.1	35.95	0.09
103	1173	nan	1330	nan	40	nan	40	nan
104	1180.75	0.13	1340.74	0.14	39.21	0.13	40.47	0.14
105	1182.09	0.11	1342.44	0.11	35.43	0.11	36.36	0.11
106	1181.37	0.13	1341.17	0.13	37.48	0.12	38.95	0.13
107	1170.71	0.12	1328.96	0.12	36.13	0.11	38.09	0.11

108	1187.41	0.17	1347.46	0.15	38.9	0.18	34.61	0.14
109	1186.48	0.15	1343.69	0.16	41.36	0.15	38.65	0.15
110	1182.73	0.14	1342.43	0.15	37.88	0.14	39.62	0.15
111	1187.7	0.19	1346.19	0.22	41.86	0.18	46.41	0.24
112	1186.47	0.16	1345.26	0.16	40.72	0.15	42.4	0.17
113	1179.54	0.19	1337.23	0.21	41.36	0.17	50.48	0.24
114	1182.41	0.16	1341.12	0.17	40.72	0.16	42.36	0.17
115	1188.05	0.18	1349.19	0.19	43.34	0.18	43.36	0.2
116	1176.16	0.17	1340.98	0.16	44.74	0.2	38.68	0.15
117	1177.4	0.17	1336.46	0.18	39.94	0.17	38.68	0.16
118	1179.27	0.12	1339.32	0.12	34.86	0.12	34.37	0.11
119	1183.95	0.14	1345.29	0.14	35.43	0.14	34.92	0.13
120	1171.23	0.71	1332.5	5.68	40	0.71	34.23	2.61
121	1168.13	0.34	1323.49	0.43	46.47	0.27	62.2	0.48
122	1177.27	0.14	1336.66	0.15	39.11	0.13	40.86	0.14
123	1179.86	0.44	1335.99	0.55	55.03	0.35	57.36	0.55
124	1178.04	0.11	1336.83	0.12	35.68	0.1	37.51	0.11
125	1177.49	0.16	1337.45	0.16	40.79	0.17	37.97	0.14
126	1178.27	0.11	1338.11	0.12	34.65	0.11	35.54	0.1
127	1174.91	0.3	1331.97	0.37	46.15	0.23	57.19	0.44
128	1179.46	0.11	1339.87	0.11	35.4	0.1	36.84	0.1
129	1182.68	0.14	1340.69	0.15	39.81	0.14	41.6	0.15
130	1188	0.16	1348.28	0.17	40.99	0.16	40.53	0.17
131	1185.34	0.24	1343.18	0.27	48.34	0.22	49.2	0.28
132	1171.13	0.52	1322.3	0.65	47.84	0.36	67.3	0.72
133	1184.61	0.16	1346.47	0.15	37.2	0.16	35.74	0.14
134	1178.51	0.38	1336.43	0.47	51.69	0.3	55.26	0.52
135	1179.93	0.11	1340.2	0.11	35.09	0.1	35.17	0.1
136	1173	0.95	1332.5	0.45	40	0.46	40	0.34
137	1176.45	0.25	1334.53	0.3	48.63	0.22	52.03	0.31
138	1175.57	0.11	1335.03	0.11	35.82	0.1	37.44	0.11
139	1173.68	0.1	1333.2	0.1	34.26	0.09	34.56	0.09
140	1177.96	0.13	1336.32	0.13	39.11	0.12	39.16	0.12
141	1173.53	0.1	1331.67	0.1	33.28	0.09	33.44	0.08
142	1184.54	0.14	1344.17	0.15	39.4	0.14	38.89	0.14
143	1190.98	0.11	1350.65	0.12	37.79	0.11	37.71	0.12
144	1183.93	0.15	1342.3	0.17	41.28	0.15	44.16	0.18
145	1185.78	0.13	1346.54	0.13	38.27	0.13	37.4	0.12

146	1181.72	0.15	1342.37	0.15	39.88	0.15	40.27	0.15
147	1184.33	0.14	1348.46	0.14	38.57	0.15	36.13	0.12
148	1182.75	0.14	1343.56	0.14	37.59	0.14	37.22	0.13
149	1179.96	0.11	1340.04	0.11	35.7	0.1	35.71	0.1
150	1178.6	0.1	1338.43	0.1	35.63	0.1	35.36	0.09
151	1173	nan	1332.5	0.57	40	nan	40	0.72
152	1178.87	0.12	1337.98	0.12	37.34	0.11	38.39	0.11
153	1178.1	0.13	1335.09	0.14	38.49	0.13	40	0.13
154	1178.81	0.2	1337.71	0.22	50.35	0.22	41.89	0.2
155	1179.72	0.22	1339.38	0.24	46.6	0.21	48.13	0.25
156	1179.21	0.18	1338.5	0.2	42.9	0.18	44.19	0.2
157	1183.56	0.16	1342.85	0.17	39.92	0.16	39.78	0.16
158	1183.85	0.21	1342.93	0.23	43.38	0.2	45.84	0.25
159	1185.06	0.12	1343.69	0.13	37.35	0.12	38.74	0.12
160	1185.01	0.18	1342.99	0.21	44.29	0.17	47.17	0.23
161	1177.75	0.11	1336.8	0.11	33.1	0.1	33.95	0.09
162	1186.1	0.17	1344.89	0.18	44.65	0.17	40.46	0.17